Soil Dynamics and Earthquake Engineering 200 (2026) 109894

Contents lists available at ScienceDirect

Soil Dynamics and Earthquake Engineering

journal homepage: www.elsevier.com/locate/soildyn

Physics-based simulation of 3D seismic site effects: Case study of the lower Sarca Valley (Trentino, Italy)

Peter Klin [a,*], Ilaria Primofiore [a,b], Luigi Zampa [a], Marco Garbin [a,c], Alfio Viganò [c], Francesco Palmieri [a], Carla Barnaba [a], Stefano Parolai [d], Giovanna Laurenzano [a]

[a] *Istituto Nazionale di Oceanografia e di Geofisica Sperimentale – OGS, Italy*
[b] *Università degli Studi "G. D'Annunzio" Chieti – Pescara, Dipartimento di Ingegneria e Geologia, Italy*
[c] *Provincia Autonoma di Trento, Servizio Geologico, Italy*
[d] *Università degli Studi di Trieste, Department of Mathematics, Informatics and Geosciences, Italy*

ARTICLE INFO

Keywords:
3D geophysical model
Seismic site response
Numerical simulation
Alpine valley

ABSTRACT

We can investigate the role of 2D and 3D geometry of sedimentary cover and bedrock topography in the seismic response of alluvial valleys and sedimentary basins by physics-based numerical simulations of seismic wave propagation in heterogeneous viscoelastic media. In this context, the present work focuses on the simulation of earthquake ground motion in the lower part of the Sarca Valley, a 5 km wide valley on the northern shore of Lake Garda in the Italian Alps. A recent study has shown that in this valley the amplitude of earthquake ground motion in the frequency range of engineering interest (0.5–10 Hz), can be amplified by a factor of up to 10 compared to rock sites. To investigate the origin of the observed amplification values, we numerically simulate the ground motion in the valley using a 3D digital structural-geophysical model created from the available geological and geophysical data. These data consist of seismic reflection profiles, interpreted geological sections and borehole measurements from existing literature, as well as data from newly conducted measurement campaigns of microtremors, shear wave velocity profiles and gravity. The level of detail that results from the constructed 3D digital model is sufficient to simulate the valley's response within the frequency range up to 5 Hz. Although the simulations performed in this work do not cover the entire frequency range of interest—extending up to 10 Hz—they nevertheless encompass the peak frequencies observed in the amplification functions at internal points within the valley. To perform the numerical simulations, we used the 3D spectral-element and frequency-wave number hybrid method, which is implemented in the latest versions of the open-source software SPECFEM3D Cartesian. We assess the capabilities of both the 3D and 1D modeling approaches to reproduce the observed seismic response within the frequency range of 0.5 Hz–5 Hz, by performing a quantitative comparison between empirical amplification functions and those obtained numerically at a selected set of locations. In particular, we considered the amplification functions evaluated from earthquake ground motion recordings at 19 locations, where a temporary seismological network operated between 2019 and 2021. The results confirm that the area is susceptible to combined 1D to 3D site effects generated by the peculiar geometry of the deposits composing the basin. The validated 3D model provides a basis for the calculation of earthquake scenarios in the area with accurate consideration of site effects from 0.5 to 5 Hz. An original aspect of this work consists in the introduction of a nine-component descriptor for site response, referred to as the site-to-site transfer function for vertically incident plane waves.

1. Introduction

Alluvial valleys and sedimentary basins are characterized by relevant seismic site effects that can significantly increase the local seismic hazard [1]. Site effects can be related to the resonance of seismic waves in the horizontal layering of the deposits [2], which we refer to as the 1D seismic response. However, lateral heterogeneities in the seismic medium can lead to site effects by focusing of the seismic wave front or by generation of surface waves [3], which we refer to as 2D and/or 3D seismic response. The 1D and 2/3D seismic responses are not mutually

---

[*] Corresponding author.
E-mail address: pklin@ogs.it (P. Klin).

https://doi.org/10.1016/j.soildyn.2025.109894
Received 23 April 2025; Received in revised form 16 October 2025; Accepted 18 October 2025

exclusive but can interact with each other to form particular seismic responses that are often observed along the edges of large sedimentary basins [4,5]. Several examples in the literature demonstrate the possibility of significant effects of the interaction between 1D and 3D responses in intermontane basins as well. Di Giulio et al. [6] explain the long duration (up to 2 min) and the high amplification (up to a factor of 20 at frequencies round 1 Hz) of low-magnitude earthquake recordings at stations in the middle of the Colfiorito plain (central Italy) with a combination of stratigraphy effect and Love waves diffracted from the basin edge. Pacor et al. and Bindi et al. [7,8] explain amplification values up to 10 in the wide frequency range 0.3–5 Hz in the Gubbio alluvial basin (central Italy) with the superposition of the stratigraphy effect and lateral propagation effects. A similar explanation is given by Bindi et al. [9] for amplification values up to 20 in the frequency range 0.5–5 Hz in the Norcia basin (central Italy).

In contrast to 1D site effects, 2D and 3D effects are characterized by a higher degree of complexity - to the point that they can also depend on the direction of the incoming seismic wave - and their quantitative prediction is a challenging task [10]. Physics-based numerical simulations of seismic wave propagation in heterogeneous media may represent a powerful approach to investigate the role of 2D and 3D geometry in the seismic response of alluvial valleys and sedimentary basins. A significant milestone in this approach consisted in the explanation of the damage belts reported after the 1995 Kobe earthquake as a consequence of constructive interference of direct s-waves with basin induced surface waves [11]. Roten et al. [12] successfully applied the 3D finite difference method to reproduce the observed site effects in the Rhone valley around the city of Sion (Switzerland) and recognized 2D resonances and edge-generated surface waves in the frequency range up to 4 Hz on the basis of an accurately defined seismic velocity model of the basin. The applicability of 3D numerical simulations for the site-specific analysis of seismic response was verified by Maufroy et al. [13], with a series of comparative exercises applied to the Mygdonian Basin (Greece), in the low to intermediate frequency range. Since then, there has been a significant increase of the use of numerical 3D simulations for analyzing site response. Thanks to 3D simulations, Cruz-Atienza et al. [14] gain new insights in the “par-excellence” site effects in the Valley of Mexico by explaining the elongation of the ground motion with the occurrence of surface wave overtones. Thompson et al. [15] demonstrated amplifications due to basin-edge effects in simulations up to a frequency of 1 Hz with 3D simulations concerning the Seattle and Tacoma basin. Hu et al. [16] applied large-scale 3D simulations to investigate the effect of topography and the superficial soil layers on the ground motion in the Los Angeles basin for frequencies up to 5 Hz. Using a validated 3D model of the Cadarache sedimentary basin in France, Castro-Cruz et al. [17] conducted a broad-band (0–10 Hz) blind prediction of ground motion at the Cadarache nuclear site for a potential Mw 6 earthquake originating from the adjacent Middle Durance fault. Large-scale 3D physics-based numerical simulations are nowadays used in Statewide California Earthquake Center (SCEC) probabilistic seismic hazard models via the CyberShake platform [18].

The reliability of numerical simulations depends strongly on the available data on the subsurface morphology and on the mechanical properties of the seismic medium. Klin et al. [19] derived a 3D seismic velocity model of a sector of the Po Valley (Italy) on the basis of geological interpretations from well-constrained geophysical data that was available thanks to hydrocarbon exploration undertaken in the area in the past decades. With that model, the 3D numerical simulations allowed the authors to explain the unexpectedly long duration of ground motion observed in the epicentral area of the 2012 Po Valley earthquake sequence with the excitation of surface waves on a buried structural ridge.

However, the use of invasive exploration methods, such as those used in hydrocarbon exploration, is not strictly necessary to produce a reliable 3D seismic velocity model for numerical simulations of earthquake ground motion. Panzera et al. [20] successfully validated a 3D seismic velocity model of the Rhone Valley around the municipality of Visp (Switzerland), which was mainly based on subsurface data obtained using non-invasive techniques.

The present work focuses on the lower part of the Sarca Valley (hereinafter LSV - lower Sarca Valley) on the northern shore of Lake Garda in the Italian Alps. According to the probabilistic seismic hazard model MPS04-S1 [21], the spectral acceleration values at rock sites in LSV for the 475-year return period range between 0.050 g and 0.075 g at the oscillation period of 1 s, between 0.150 and 0.175 g at 0.5 s, and between 0.3 g and 0.35 g at 0.2 s. These seismic hazard values are relatively low compared to other locations in Italy. A recent study carried out as part of the project “Studio riguardante la risposta sismica locale del tratto terminale della valle del fiume Sarca in prossimità del Lago di Garda” has shown that at sites inside LSV amplifications of earthquake ground motion of up to 10 in the frequency range of engineering interest (0.5–10 Hz) are possible in respect to a rock site [22]. This fact indicates that the actual seismic hazard in the LSV could be significantly higher and requires an accurate assessment, as the valley is populated and hosts several economic activities.

In the framework of the same project, which was based on non-invasive techniques, Parolai et al.[23] applied seismic noise interferometry to demonstrate the existence of non-negligible cross-coupling between the components of ground motion at some locations within the LSV and at a nearby rock site. According to Paolucci [24] the cross-coupling is associated with lateral heterogeneities in the mechanical properties of the soil. This suggests that the origin of the amplification in LSV cannot be fully explained by 1D stratigraphic resonance and that we also need to consider 3D effects.

To better understand the origin of the observed site response in the about 5 km wide LSV, we use the available geological and geophysical data and build a 3D digital structural-geophysical model using GeoModeller® software [25]. The used data consists of seismic reflection profiles, interpreted geological sections and borehole measurements from existing literature, as well as data from newly conducted measurement campaigns of microtremors, shallow shear wave velocity profiles and gravity. To perform the numerical simulations we adopt the 3D spectral-element and frequency-wave number hybrid method [26], that is implemented in the latest versions of the open-source software SPECFEM3D Cartesian [27]. We demonstrate the efficiency of the resulting 3D model in simulating the ground motion variability within the LSV, in the frequency range up to 5 Hz, by a quantitative comparison between the empirical and the numerically evaluated amplification functions at the same site. In particular, we consider the amplification functions evaluated with the Generalized Inversion Technique (GIT) from earthquake ground motion recordings at 19 sites, where a temporary seismological network operated between 2019 and 2021 [22].

Numerous studies on site effects have documented random event-to-event variations in seismic response at a single location, a phenomenon referred to as within-site variability [28]. This variability reflects an inherent uncertainty in site response, largely attributed to the sensitivity of the response of three-dimensional subsurface heterogeneities to the azimuth, angle of incidence, and polarization of incoming seismic waves (e. g. Ref. [29,30]). Consequently, site response may be influenced by the location and mechanism of the seismic source, as well as by source-to-site path effects. These findings challenge the classical source–path–site paradigm, suggesting that site response cannot be considered entirely independent of the characteristics of the seismic input, even in the linear regime associated with weak ground motions. In the present study, however, we did not investigate the dependence of site response on the relative position of the seismic source. Our objective was to assess whether the constructed 3D model is capable of reproducing the average site response derived with GIT, under the simplifying assumptions of the classical source–path–site framework. A more detailed analysis of site response variability in relation to source characteristics is planned for future work.

An original aspect of the present work is the approach we use to determine the seismic response with numerical simulations. To account for the cross-coupling effect we define a 9-component descriptor for the site response, which we refer to as the *site-to-site transfer function* for vertically incident plane waves. To evaluate this descriptor, we excite the seismic wavefield in the 3D domain with vertically incident plane waves polarized in the three fundamental directions.

The article is organised as follows. After an overview of the geological and seismotectonic features of the valley, we describe the construction of the model and the setup of the numerical simulations. For the sake of brevity, we present the procedure for evaluating the site-to-site transfer function from numerical simulations in the appendix of the article. In the last part of the article, we validate the constructed model by comparing simulations and observations. The study confirms that the deposits that make up the basin cause combined 1D to 3D site effects. The validated 3D model forms the basis for the calculation of earthquake scenarios in this area.

2. Geological and seismotectonic setting

The LSV is located in southern Trentino (northern Italy) at the northern termination of Lake Garda (Fig. 1). This NNE-SSW oriented valley has a steep-walled structure which is dominated by rocks of Mesozoic to Cenozoic age [31]. About the Lower-Middle Jurassic rocks units, a clear differentiation between the western and eastern portions of the area is evident [31,32]. West of Riva del Garda, the platform (Corna limestones) and basinal units (Tofino Formation) belonging to the so-called Lombardian Basin. East of Riva del Garda, the Calcari Grigi rocks deposited on the Trento (Venetian) platform during the Early Jurassic. These two paleogeographic domains are separated by the Ballino-Garda paleo-fault system (BG in Fig. 1) [33]. Around the southernmost termination of the Sarca Valley, between Arco and Riva del Garda, younger rock units crop out. They are mainly represented by Cretaceous micritic limestones (Maiolica and Scaglia Rossa) and by Eocene platform carbonates (Malcesine and Nago limestones) [31]. The youngest bedrock units are sandstones of Late Oligocene-Early Miocene age (Monte Brione Formation), which form the summit of Monte Brione between Riva del Garda and Nago-Torbole. Moreover, a thick Quaternary cover is present, reaching about 400 m depth at Riva del Garda [34]. These sediments are of glacio-lacustrine [35] or alluvial origin (Sarca River and other minor tributaries; [31]).

Both the bedrock structure and the shape of the buried valley are strongly asymmetric, because of the regional structural setting. In fact, the Giudicarie fault system acted since the Late Cretaceous as a regional transfer zone, with the generation of a well-developed NNE-SSW oriented fold-and-thrust belt with great morphological evidence (Fig. 1) [32,33]. In the study area, this is particularly evident considering the NNE-SSW directed valley orientation, the presence of gently dipping beds on the eastern flank of the valley, or the asymmetric shape of its buried bottom [34]. In addition, the NW-SE Schio-Vicenza strike-slip fault system is particularly developed, which cross-cuts the older Giudicarie fault system (SV in Fig. 1) [32]. Besides surface geology, also upper crustal velocity anomalies are correlated in shape, orientation and thickness with these major fault systems [36].

About seismicity, southern Trentino is seismically active, both in the Lake Garda area and the lower Adige Valley (Fig. 2). A comprehensive view of the historical and instrumental seismicity is available in Guidoboni et al. [37] and Viganò et al. [38], respectively. This is due to the present deformation acting at upper crustal levels in the Giudicarie seismotectonic domain (hypocentres at 0–15 km of depth), where compression is still active today and moderate earthquakes occur (e.g., November 24, 2004, ML 5.2, Salò; [39], 2015). In particular, the Giudicarie fault zone, comprised between the Po plain and the inner Alpine chain, is seismically active only along its southern portion (Lake Garda area), while northward seismicity is rather scarce. In this view, the transition zone exactly coincides with the lower Sarca Valley [36]. Here, a moderate earthquake struck Riva del Garda and its surroundings (December 13, 1976, M_L 4.3, Ledro, Fig. 2). Using a new location approach proposed by Viganò et al. [40], it was possible to associate this seismic event to the same source that generated an earthquake swarm during 2015 (maximum M_L 4.1).

3. Definition of the 3D geophysical digital model

The basic step for physics-based numerical simulation of earthquake ground motion is the creation of a digital model of the 3D subsurface structure by integrating the available geological and geophysical data with a computer-aided method. For this purpose, we used the commercial software Geomodeller [25]. The procedure works on the basis of

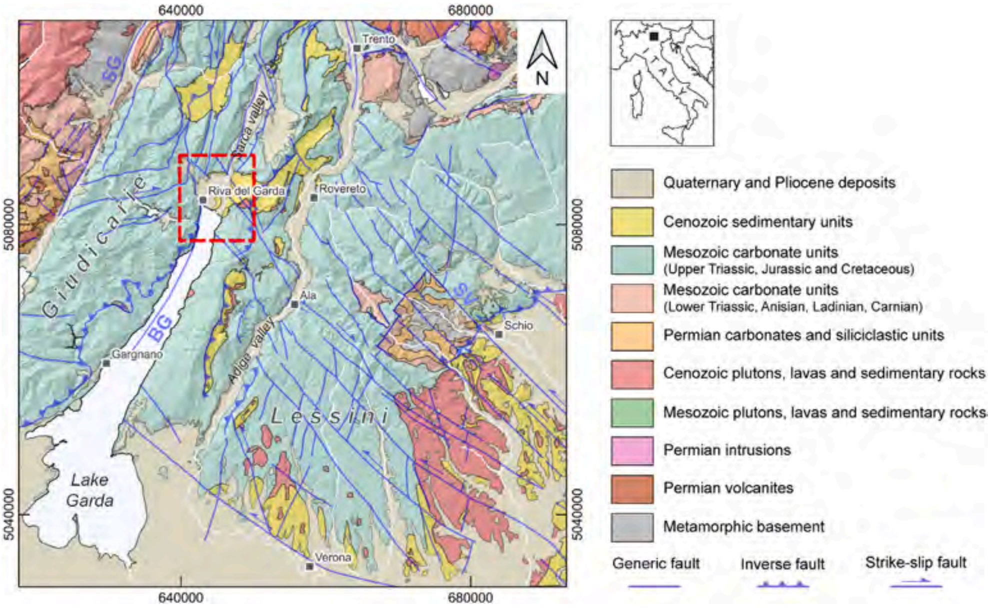

Fig. 1. Geological map of the investigated area surroundings. Map data from CARG project database (https://www.isprambiente.gov.it/en/projects/soil-and-territory/carg-project-geologic-and-geothematic-cartography) and other original cartographies. The red rectangle delimits the area under investigation in this article. (For interpretation of the references to colour in this figure legend, the reader is referred to the Web version of this article.)

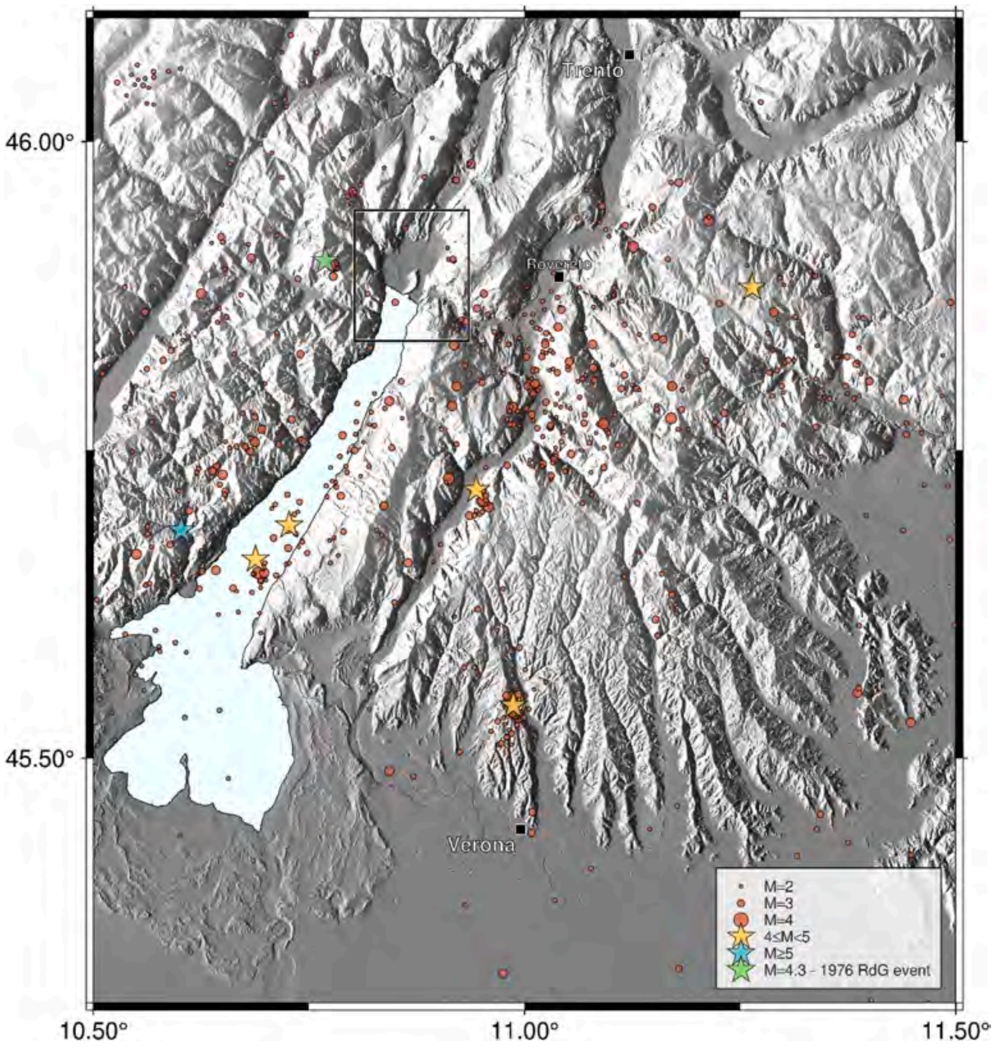

Fig. 2. Epicenters of events with magnitude M $\geq$ 2 that occurred in the surroundings of the study between 1985 and 2025 (https://rts.crs.inogs.it/). The light-green star marks the epicenter of the Ledro (or Riva del Garda – RdG event) earthquake of December 13, 1976 (see text for details). (For interpretation of the references to colour in this figure legend, the reader is referred to the Web version of this article.)

the interpolation of potential fields [41], and results particularly effective for introducing constraints in the model like those obtained by primary geologic data such as lithological contacts, deposits and boreholes, or those derived by using classical stratigraphic rules and temporal relationships between faults and formations. We have defined the digital 3D model to a depth of 1400 m below sea level over the rectangular area shown in Fig. 1 with an extension of 10 km in east-west direction and 12 km in north-south direction. The area is centered on Monte Brione and includes the alpine valley on the northern shore of Lake Garda (65 m above sea level) and hills up to 1600 m above sea level.

To create the 3D digital model, we have taken into account data from the literature and from the investigations carried out as part of the recent seismological study to determine the seismic response of the area [22].

The data from literature consists in:

- the Digital Elevation Model with a resolution of 10 m [42];
- the bathymetry and the uppermost stratigraphy of the Lake Garda [43];
- the Geological Map of Servizio Geologico of Provincia Autonoma di Trento (hereafter PAT), sheets 80060, 80070, 80080, 80100, 80110 and 80120, at a scale of 1:10,000 (https://www.provincia.tn.it/News/Approfondimenti/Carta-Geologica-della-Provincia-Autonoma-di-Trento);
- the Geological Map of Italy, sheet 080 “Riva del Garda”, and the geological section C-C′, at a scale of 1:50,000 (https://www.isprambiente.gov.it/Media/carg/80_RIVA_DEL_GARDA/Foglio.html);
- a seismic profile and deep drilling data performed by the Geological Service of PAT [34];
- boreholes collected by the PAT geocartographic portal (http://www.territorio.provincia.tn.it/portal/server.pt/community/sondaggi/771/surveys/21171);
- a borehole in the hamlet of Linfano [44];
- a audio-magnetotelluric (AMT) section created along the shore of Lake Garda (Garbari, personal communication);
- a vertical seismic profile (VSP) [45].

The data obtained within the project (see Fig. 3) consists in:

- the depth of the seismic bedrock derived from Horizontal-to-Vertical Spectral Ratios (HVSR) of microtremors at 109 locations;
- shallow S-wave velocity profiles derived from the Multichannel Analysis of Surface Waves (MASW) performed at 6 locations;
- the results of a gravity survey performed at 295 locations.

and is described in the following subsections.

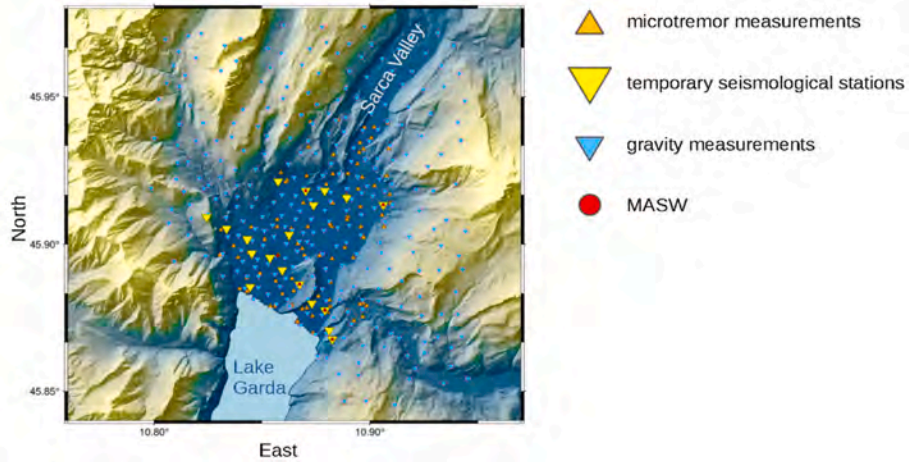

Fig. 3. Map of the measurement points considered in a recent investigation [22], to determine the seismic response of the area.

3.1. Soil thickness estimation form seismic noise HVSR

It is well known that the position of the peak in the seismic noise HVSR can provide a good estimate of the resonant frequency f_0 of the seismic response of the site if there is a strong impedance contrast between the soil and the underlying rock.

Thanks to the extensive campaign of microtremor measurements in the study area [22], we have access to a comprehensive map of the distribution of f_0 in LSV. The map on the left in Fig. (5) represents an interpolation of the f_0 values determined at the microtremor measurement points indicated in Fig. (3). From the map we can recognize a central area north-east of Riva del Garda with f_0 values below 1 Hz and an area east of Monte Brione with f_0 values between 1 and 5 Hz. Valley edges and slopes tend to have high resonance frequencies (f_0 of the order of 10 Hz), or exhibit a flat HVSR curve, indicating a negligible thickness of the sediment cover.

According to Ibs-von Seht and Wohlenberg [46], f_0 correlates with the soil thickness H via the relationship

$$H(f_0) = af_0^b, \tag{1}$$

where the values of the parameters a and b are related to the dependence of the shear wave velocity on the depth in the soil layer, which we assume to be the same across the area covered by sediments. So far, the relation expressed in Eq. (1) has been considered in a number of studies, starting with Parolai et al.[47], who obtained a clear correlation between resonance frequency and sediment thickness derived from 32 boreholes reaching the bedrock in the Cologne area (Germany). Thabet [48] provided a comparison of the values of the parameters a and b that were retrieved using borehole data at KiK-NET seismological stations with the results of other valuable studies in bibliography that involved the fitting of Eq. (1), finding that geological conditions at the site have a strong influence on the resulting frequency–depth relationship. For this reason we decided to perform a nonlinear regression fit of Eq. (1) specific for LSV, by using the soil layer thickness from the deep drilling data located in the center of the valley [34] and from shallower boreholes and seismic profiles located close to the valley [49] at the points shown in

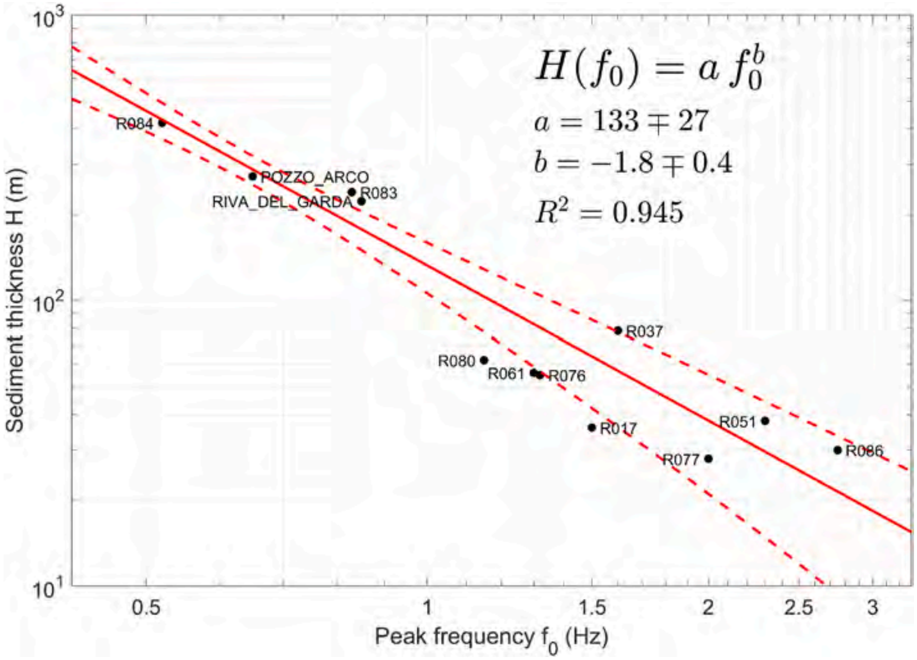

Fig. 4. Scatter plot of sediment thickness as a function of HVSR peak frequency, the corresponding regression curve and the values of the coefficients together with the 95 % confidence interval. The labels indicate the measurement locations shown in the map in Fig. 3.

Fig. 5 (left). The points in Fig. (4) denote the sediment thickness H in function of the value of f_0 measured in situ from microtremor HVSR, and the red line denotes the regression curve on logarithmic scale. The regression coefficients are given along with the 95 % confidence intervals. The high value of the coefficient of determination R^2 supports the applicability of the relationship in Eq. (1) to the case of LSV. Since Eq. (1) assumes lateral homogeneity of the sediment fill, we can interpret the scatter of the data points with respect to the regression curve (the residual reaches a value of up to 40 % for site R017) as a consequence of the presence of lateral heterogeneities in the internal structure of the soil.

As shown in Ibs-von Seht and Wohlenberg [46] and in a number of follow-up studies (e. g. Ref. [50]; e. g. Ref. [20]), once we have determined the parameters in Eq. (1), we can apply it to mapping the indicative thickness of sediments using the f_0 map from microtremor measurements. In Fig. 5 (right) we display the map of the estimated thickness H of the deposits layer in LSV obtained from the map of the resonance frequencies f_0 in Fig. 5 (left).

3.2. Shallow S-wave velocity profiles from MASW

We estimated the S-wave velocity (V_S) profile in the shallow subsurface using the MASW technique [51] at 6 out of 19 locations of the temporary seismic network. We selected these locations to investigate different possible site conditions in the study area. In detail, we have considered one site on deep soils in the centre of the main valley (station TN04, see Fig. 3), two sites on the eastern and western edges of the valley (stations TN16 and TN18 respectively), one site in the alluvium of the tributary valley (station TN05), one site on sandstone outcrops on Monte Brione (station TN06) and one site on limestone (station TN02). At each investigated site, the acquisition layout consisted of 17 vertical 4.5 Hz geophones in a linear array. Multiple shots were recorded at each site, with the seismic source positioned on either side of the profile. As seismic sources, we used either a 4-kg hammer striking vertically on an iron plate on the ground or a 180-kg drop weight. Profiles length spanned from 120 m to 50 m, on soils and rock, respectively.

The S-wave velocity vertical profiles were obtained by applying a genetic algorithm to the joint inversion of surface wave dispersion curves obtained from MASW and microtremor HVSR [52,53]. The results (Fig. 6) provide valuable clues for the near-surface characterization of the digital model. In particular, we can see that in the uppermost hundred meters the sites on sediments (TN04, TN05,TN16 and TN18) are characterized by an average V_S value in the order of 450 m/s. For the rock sites (TN02 and TN06) instead, there is evidence for a superficial weathering layer, about 30 m thick and with an average V_S value of the order of 1000 m/s, overlying the more compact rock with higher V_S values.

3.3. Gravity survey

The gravity survey covered an area of around 120 km^2, with 295 evenly distributed measurement points with an average spacing of 500 m ensuring a high and homogeneous spatial resolution (Fig. 3). We performed the measurements with a ZLS Burris gravity meter, which employs a Zero Length Spring (ZLS) system in combination with a feedback mechanism to increase stability and minimize instrumental drift. The acquisition strategy allowed for adequate monitoring of instrumental drift, which generally remained within ±0.01 mGal, as well as the assessment of final closure errors.

The processing of the gravity field data involved several correction steps. We calculated the Bouguer anomaly (Fig. 7a) according to standard procedures [54,55]. We applied terrain correction using vertical right prisms [56], accounting for effects up to 25 km with curvature correction beyond 18 km, using digital terrain models (DTM) with different cell sizes based on the distance from the gravity station. Given the presence of Garda Lake, we applied a bathymetric correction to accurately account for the water masses, using bathymetric data from Gasperini et al. [43]. The residual anomaly exhibits a strong correlation with the surface geology, showing negative values over sediment infill (low densities) and positive values over rocky outcrops (high densities) (Fig. 7c). To further refine the analysis, we applied a terracing operator [57] to emphasize sharp density boundaries, which in this case are directly related to the lateral contacts between bedrock and sediment. This operator highlighted several signals that indicate possible subsurface density variations in the valley itself. In particular it highlighted the possible continuation of the Monte Brione outcrop in a northeasterly direction, where the rock mass appears beneath the sediments (Fig. 7d).

We created a 3D density model of the area from the gravity anomaly through a supervised optimization based on a combination of forward and inverse modelling. We performed forward modeling using IGMAS+, a 3D gravity modeling tool based on polyhedral representations of subsurface structures [58] whereas we used GRAV3D [59] for the inversion. We derived the initial geometry of the valley from the bottom depth of sediments estimated by the microtremor HVSR analysis

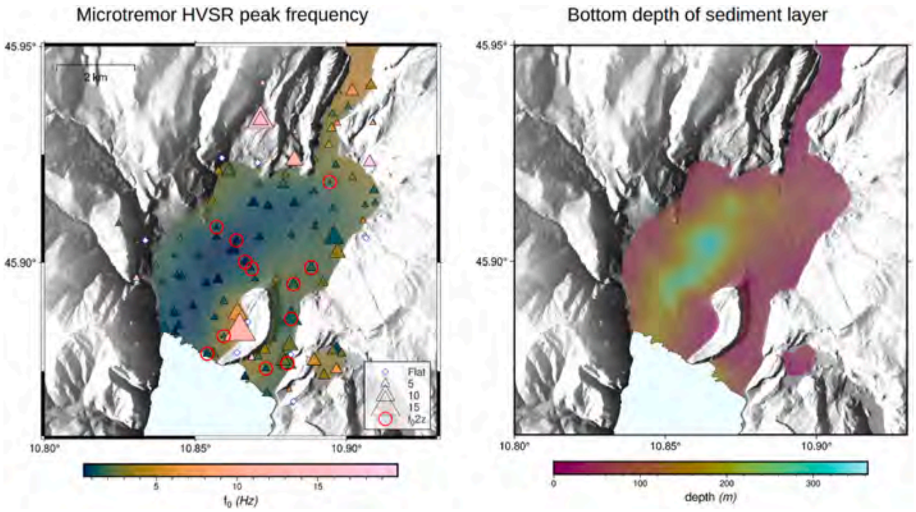

Fig. 5. Left: modified from Laurenzano et al. [22], map of resonance frequencies deduced from microtremor HVSR in the valley. The triangles show the position of the measurement points. The size of the triangles is proportional to the HVSR peak value. At the points circled in red, the depth of the sediment layer was known from borehole or seismic data. Right: bottom depth of the sediment layer in the valley according to the power law determined in the present work (see Fig. 4). (For interpretation of the references to colour in this figure legend, the reader is referred to the Web version of this article.)

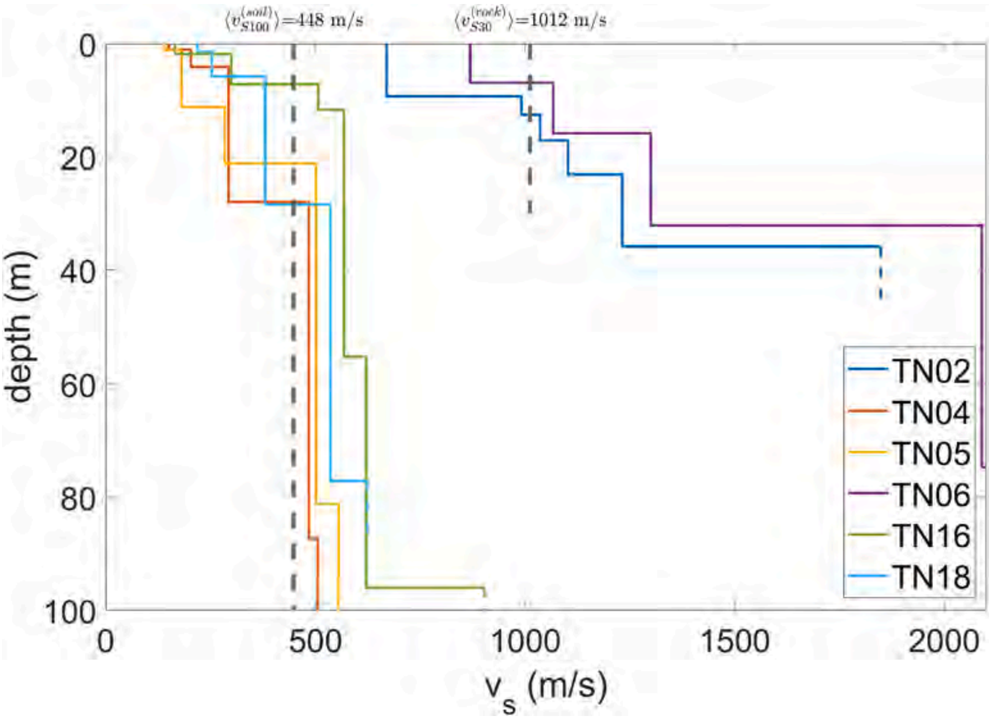

Fig. 6. Shear wave profiles at 6 selected sites in the studied area (Fig. 3), as resulting from MASW inversion. The resulting average v_{s100} value for the sites on soil and the average v_{s30} value for the sites on rock are also shown.

(subsection 3.1 in this article) and we assigned 2.2 g/cm^3 and 2.6 g/cm^3 to the initial average density of the sediments and the bedrock, respectively. We refined locally the bottom depth of sediments using the interactive tools of IGMAS + to improve the fit between the calculated and observed gravity data. On the other hand, we applied the inversion to optimize the density distribution without affecting the buried shape of the valley.

The inferred valley morphology shows a well-defined buried depression that reaches a maximum depth of about 400–450 m, which is largely consistent with earlier interpretations. The inverted density distribution does not show a sharp boundary between the unconsolidated sediments and the bedrock, but rather indicates a gradual transition zone where the top of the bedrock can be recognized in a density range of 2.4–2.5 g/cm^3 (Fig. 8c and d). We observe the largest deviations, up to ± 1 mGal, where the bedrock outcrops, e.g. along the eastern ridges and at the summit of Monte Brione (Fig. 8b). These deviations are probably due to local density variations in the rock formations, which we did not take into account when optimising the model. Overall, the representation of the subsurface structure of the valley obtained from gravity data is consistent with the sediment bed depth determined from microtremor HVSR (Fig. 8c and d).

3.4. The set-up of the model

The first step in building the model is to define a stratigraphic pile with the different units that make up the volume under investigation on a geological basis. For this purpose, we have divided the valley sediments into two units, one with recent alluvial deposits and one with older heterogeneous (lake/glacial/alluvial) deposits. On the other hand, we have considered three different rock units. Two of them reflect the distinction between the area west (Lombard Basin) and east (Trento/Venetian Platform) of the Ballino-Garda Fault, while a third rock unit consists of the sandstone formations outcropping on Monte Brione. The water of the lake forms the sixth unit.

To constrain the geometry of the geological bodies, we used:

- manually digitized interfaces between the geological formations resulting from the excerpt of both the cited geological map and geological cross-section;
- thickness of the valley deposits as estimated from the peak frequencies of microtremor HVSR (subsection 3.1);
- local discontinuities resulting from boreholes and other geophysical/geological surveys.

We have built the model in several steps by gradually integrating the available data from the surface. At each step, we calculated the implicit surfaces of the formation boundaries and checked the partial result before adding new elements. We show a view on the final 3D geological model in Figs. 9 and 10.

In order to perform the physics-based numerical simulation of seismic wave propagation, we need to assign the values of the involved physical properties to each point in the 3D spatial domain. We assumed that the material composing each unit consists in a uniform isotropic and viscoelastic medium described by the following quantities: the velocities V_P and V_S of the compressional and shear waves, respectively, the mass density ρ and the elastic quality factors Q_K and Q_μ for bulk and shear deformations, respectively.

The distinction among the bedrock units associated with the Lombardian Basin, the Trento Platform, and the Monte Brione Sandstones, as depicted in the 3D model (Fig. 9), is based primarily on paleogeographic criteria. In practice, however, these structural units are neither internally homogeneous nor defined by consistent physical properties. According to the consulted geological map [31], these three structural units encompass more than a dozen distinct geological formations. Most of these formations consist of limestone, a rock type known for its highly variable mechanical properties (e. g. Ref. [60]), which makes it challenging to assign adequate mechanical characteristics to each unit. Therefore, for the sake of simplicity—and exclusively for the purposes of the numerical simulation—we opted to represent the bedrock as a single, generic rock unit with homogeneous properties, effectively merging the three rocky structural units in the model. This simplification implies that the simulation does not account for potential

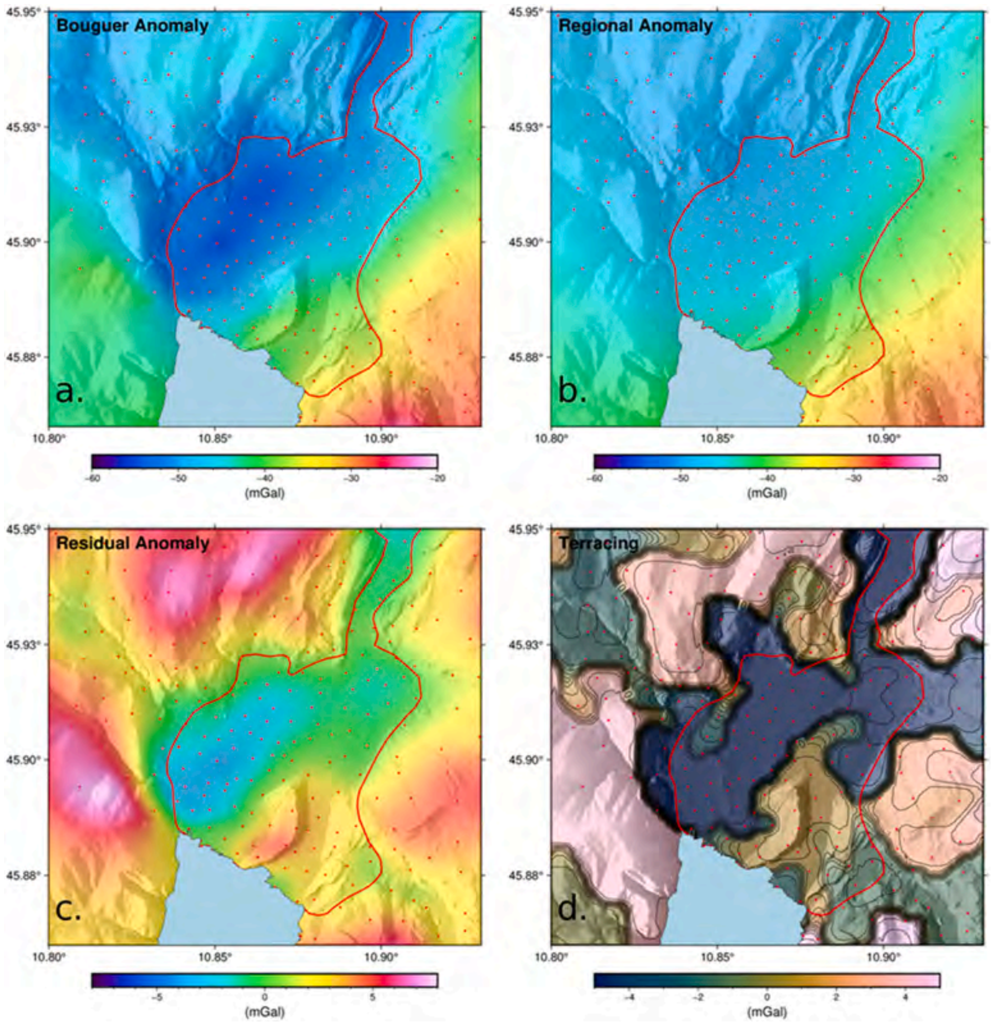

Fig. 7. Gravity anomaly maps. (a) Bouguer anomaly, (b) regional component, (c) residual anomaly after removing the regional trend, (d) terracing operator that emphasises the anomaly over lateral density contrasts. Red dots show the positions of the gravity measurements across the area, and the red boundary line indicates the limits of the data used for modelling. (For interpretation of the references to colour in this figure legend, the reader is referred to the Web version of this article.)

effects arising from heterogeneities within the bedrock structure. However, it is assumed that the seismic response is primarily governed by the geometry of the basin and the seismic velocity distribution within it, which justifies this modeling choice.

The parameter values assigned to the bedrock structural unit (see Table 1) were determined as follows. The mass density is consistent with the gravimetric study (see Section 3.3). The compressional wave velocity (Vp) was derived as the average of laboratory measurements carried out by the Geotechnical Laboratory of the Geological Survey of the Autonomous Province of Trento. These measurements were performed on limestone core samples obtained from boreholes at depths ranging from 40 to 90 m, within the context of engineering works on the eastern side of Lake Garda. The shear wave velocity (V_S) was assigned by applying a V_P/V_S ratio of 1.8.

To represent the lower seismic velocities close to the surface of the rocky formations, which were highlighted by the MASW results (subsection 3.2) we have introduced a thin layer of weathered bedrock covering all outcropping limestones and sandstones.

The density values assigned to the two soil structural units (see Table 1) were obtained from the gravimetric study (see Section 3.3), while the seismic wave velocities were derived from a technical report describing the Vertical Seismic Profile conducted along the Pozzo Arco borehole, located in the central part of the valley's western section [45] and from MASW surveys carried out at various locations across the valley (Fig. 6).

Even though the lake water is included in the 3D model as a structural unit (Figs. 9 and 12), we chose to simplify the simulations by assigning the water the same properties as the soft deposits and excluding from the analysis the solution on the water surface. This decision stems from the gentle slope of the lakebed near the northern shore [43], which poses challenges for adequate mesh discretization and is unlikely to generate significant physical effects that would influence the seismic response inland. Although recent studies have investigated seismic responses at the waterbed of alpine lakes —which are often characterized by huge amplification (e. g. Ref. [61]) — our study focuses exclusively on inland sites.

The values assigned to the physical quantities in the adapted 3D model are listed in Table (1). The values of shear quality factors are estimated as $Q_\mu = 0.1 v_S$ according to a widely used rule of thumb (e. g. Ref. [62]), whereas the bulk quality factor is set as $Q_K = 3.5\ Q_\mu$ in accordance with the theory exposed by Morozov [63].

4. 3D numerical simulation of the site amplification

4.1. Site-to-site transfer function

In this study we neglect possible non-linear effects in the seismic response, as it is based exclusively on observations of weak ground

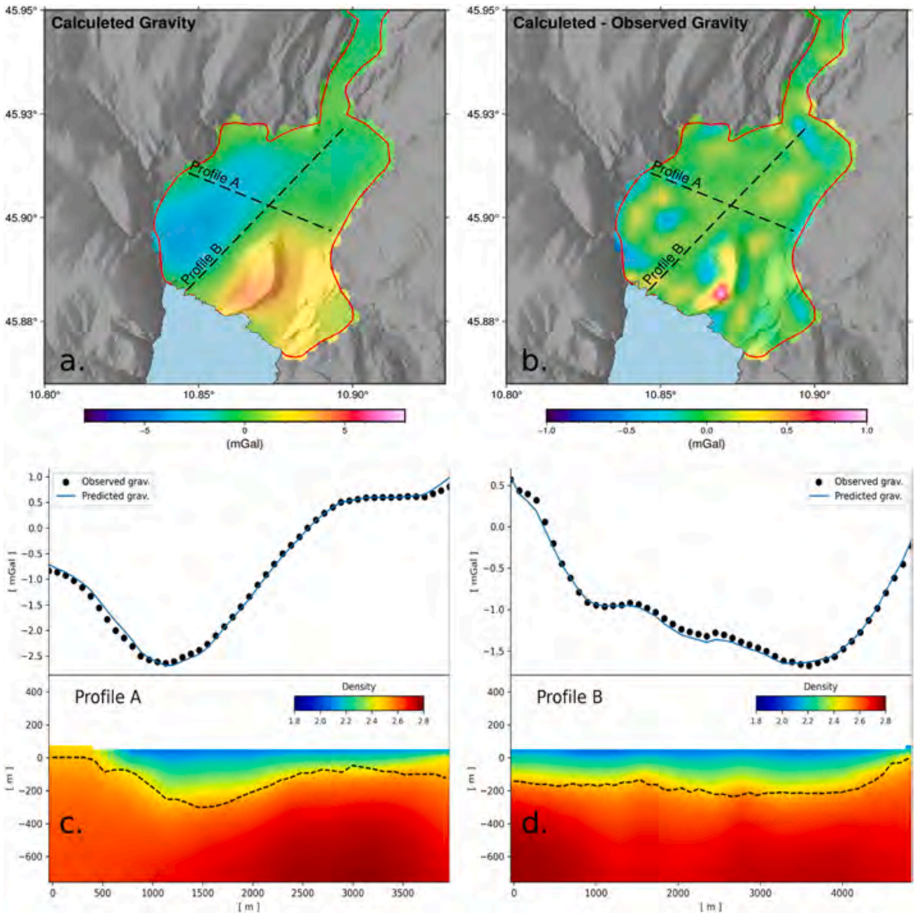

Fig. 8. Gravity anomaly of the inverted 3D density model (a) and differences with the observed residual gravity (b). Density profiles from the 3D inverted gravity model along the E-W direction (c) and the SW-NE direction (d). The red line marks the extent of the gravity data used for modelling, while the black dashed lines in the panels (c) and (d) indicate the bottom depth of sediments as obtained from microtremor HVSR. (For interpretation of the references to colour in this figure legend, the reader is referred to the Web version of this article.)

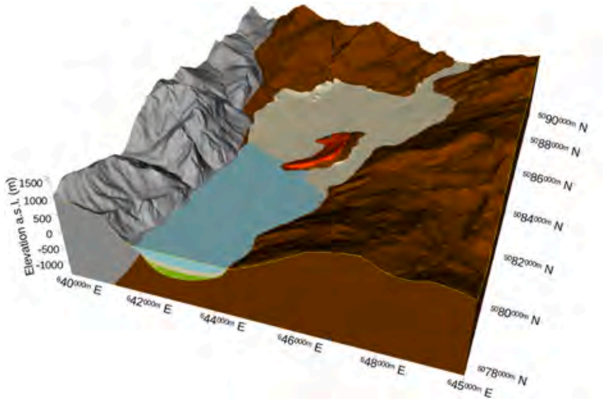

Structural unit	*color*
Lombardian Basin limestones	⬜
Trento platform limestones	🟫
Monte Brione sandstones	🟧
Heterogenic (stiff) deposits	🟩
Alluvial (soft) deposits	⬜
Lake water	🟦

Fig. 9. Full view of digital 3D model with 6 structural units.

motion data. Even if it is strictly linear, the retrieval of the amplification function from the 3D model is not straightforward, because when we consider a heterogeneous 3D medium, the characterization of the site response must take into account the cross-coupling between all three motion components at the investigated site and those at the reference site [23,24]. In the present work, we employ 3D physics-based numerical simulations of plane waves with vertical incidence to define a site-to-site 9-component complex valued transfer function with components $T_{ij}(\boldsymbol{x},\boldsymbol{x}_0,f)$. This function permits to express the 3-component vector $\boldsymbol{u}(\boldsymbol{x},t)$ describing the ground motion at a generic site $\boldsymbol{x}$ in function of the ground motion $\boldsymbol{u}(\boldsymbol{x}_0,t)$ at the reference site $\boldsymbol{x}_0$, when both sites are affected by the same incoming vertically incident input motion $\boldsymbol{u}^{INP}(t)$, as schematized in Fig. (11).

If we denote with $F\,[-]$ the Fourier transform operator, the relation between the three-component output motion at the two sites can be expressed as:

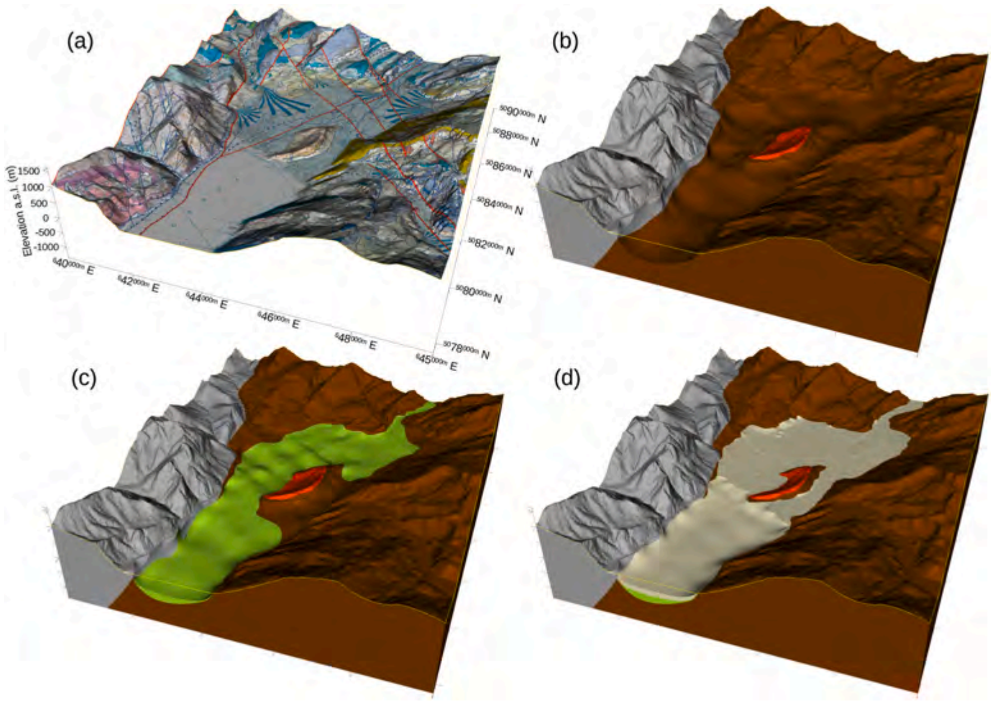

Fig. 10. Partial views of digital 3D model. a) topographic surface with geological map superimposed. b) Limestones and sandstones units only. c) Heterogenic deposits above bedrock. d) Alluvial deposits above the remaining units except water.

Table 1
Values of the physical properties of the structural units that are considered in 3D numerical simulations. The maximum thickness (extension in the vertical direction) is also listed.

	ρ (kg/m^3)	v_P (m/s)	v_S (m/s)	v_P/ v_S	Q_κ	Q_μ	*Max. thick. (m)*
Bedrock (limestones and sandstones)	2600.	4500.	2500.	1.8	875.	250.	∞
weathered bedrock	2000.	2000.	1000.	2.0	350.	100.	30.
stiff deposits (old heterogenic)	2300.	2175.	950.	2.29	350.	100.	310.
soft deposits (recent alluvial)	2000.	1825.	450.	4.05	175.	50.	160.

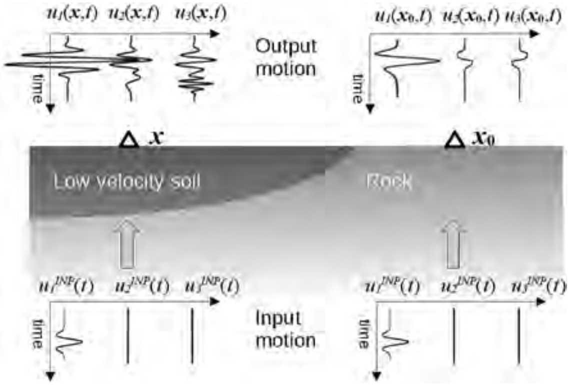

Fig. 11. Explanatory illustration of the components of input and output motion in the definition of the site-to-site 9-component complex valued transfer function.

$$F[u_i(x,t)] = \sum_{j=1}^{3} T_{ij}(x,x_0,f)F\left[u_j(x_0,t)\right] \tag{2}$$

or

$$F[\boldsymbol{u}(x,t)] = \mathbf{T}(x,x_0,f)F[\boldsymbol{u}(x_0,t)] \tag{3}$$

in matrix notation (with bold italic denoting 3-component column vectors and bold roman denoting 3x3 matrices). In the Appendix of this article, we discuss the theoretical and practical aspects for the evaluation of $\mathbf{T}(\boldsymbol{x}, \boldsymbol{x_0}, f)$ from a digital 3D model by using physics-based numerical modeling of seismic wave propagation. Once the transfer function $\mathbf{T}(\boldsymbol{x}, \boldsymbol{x_0}, f)$ is obtained from numerical simulations, we can predict the ground motion in the generic point $\boldsymbol{x}$ of the spatial domain for any "reference" ground motion assigned to the reference site $\boldsymbol{x_0}$, without having to run the numerical simulations again, but only by applying Eq. (3). The ground motion assigned to $\boldsymbol{x_0}$ may or may not be a record that we collected at site $\boldsymbol{x_0}$. It may be a record conveniently selected from ground motion databases, or it could be a simulated record derived from numerical modeling on a larger spatial scale, where we have considered the effects of earthquake source and wave propagation through the crustal structure, but neglected the local detail-driven site effects.

4.2. *Computation of the numerical solution*

In order to compute $\mathbf{T}(\boldsymbol{x}, \boldsymbol{x_0}, f)$ from a 3D model, we can choose from a number of affirmed numerical methods for the computation of the propagation of seismic waves in 3D heterogeneous media (see e. g. Ref. [13]). Considering the geometrical complexity of the 3D model of LSV we decided to perform the numerical modeling by relying on the spectral element method (SEM). SEM was first introduced in the study of acoustic and elastic waves by Seriani and Priolo [64] and combines the geometrical flexibility of Finite Elements Methods (FEM) with the accuracy of the spectral methods. In our study we relied on the software SPECFEM3D *Cartesian* [27]. The SPECFEM3D code takes into account the intrinsic attenuation properties of the viscoelastic medium [65] and allows for the coupling with the frequency wavenumber (FK) method [26], with which we can efficiently model the incoming of a plane wave into the domain, as requested in the evaluation of $\mathbf{T}(\boldsymbol{x}, \boldsymbol{x}_0,f)$. The usage of the SPECFEM3D code is well established in the field of computational seismology, (there are about 200 publications concerning studies performed with that software, which have received at least 10 citations in the last 5 years), especially in applications concerning engineering seismology (e. g. Ref. [66–69]).

One of the most critical parameters to define, when planning a numerical simulation of seismic wave propagation using a digital 3D model, is the upper frequency limit, $f_{\max}$. Beyond its implications for the computational cost of the sumulation, $f_{\max}$ governs the spatial resolution required in digital 3D models to accurately simulate the influence of structural details. Due to limited data for a more detailed characterization of the velocity profile throughout the study area, the internal structure of the valley in the constructed 3D digital model was simplified to comprise just two homogeneous structural units. Based on this simplified velocity structure, the 1D amplification functions calculated beneath the stations located within the valley show a dominant peak in the frequency range below 5 Hz. Consequently, we adopted 5 Hz as the value for $f_{\max}$ in our simulations.

In order to obtain accurate solutions with SEM, we need to discretize the spatial domain into a set of non-overlapping hexahedral elements with size smaller than or equal to the local minimum S-wavelength [70].

We employed the internal mesher of SPECFEM3D to generate a computational mesh with element sizes on the order of 25 m, which is well below the threshold determined by the minimum S-wave wavelength of 90 m. This resolution ensures accurate wavefield representation and satisfies the spatial discretization requirements. The resulting simulation domain (Figs. 12 and 13) comprises approximately 8 million elements. To meet the Courant–Friedrichs–Lewy (CFL) stability condition and minimize numerical dispersion, the time step was set to 0.0002 s. Additionally, a preliminary test was conducted on a homogeneous domain with flat topography to verify the correctness of the simulation setup.

Simulating 24 s of seismic response (equivalent to 120,000 timesteps) to an incident plane wave required approximately 5000 core hours on the Leonardo high-performance computing (HPC) system at CINECA, equipped with Intel Xeon 8480+ processors. The computation was accelerated through MPI-based parallelization, enabling efficient distribution of the workload across multiple cores. To evaluate the full 3D transfer functions for incident plane waves (see Appendix), we needed to perform a simulation for each of the three cases of impulsive plane waves polarized in the East-West, North-South and vertical directions.

4.3. Comparison between simulations and observations

The validity of digital models of the Earth's subsurface, used in physics-based ground-motion simulations, is typically assessed through quantitative comparisons between numerically simulated seismic traces and actual earthquake recordings [13]. This approach generally requires that the spatial domain of the simulation include the source location of each modeled event, with both the source location and mechanism being well constrained. Consequently, the validation process extends beyond site response to include the accurate modeling of seismic wave generation at the source and its propagation through the upper crust. However, ground-motion predictions for shallow earthquakes at short epicentral distances are particularly sensitive to uncertainties in source location [71], which can pose significant challenges to this approach.

As this study focuses exclusively on site response, we adopted an approach that avoids issues related to uncertainties in source location, source mechanism, and source-to-site path effects. Specifically, we employed site-to-site transfer functions based on the assumption of a vertically incident plane wave (see Section 4.1). While the incoming wavefront of a local earthquake is neither strictly planar nor perfectly vertically incident, this simplification is widely accepted in site effects analyses (e. g. Ref. [72]) and is also used in the interpretation of earthquake recordings within the framework of the diffuse field theory [73].

Importantly, the plane wave assumption implies that site amplification is independent of both the source location and the source-to-site propagation path, making it consistent with generalized inversion techniques (GIT) commonly used to estimate site amplification from earthquake recordings (e. g. Ref. [74]). Given that the seismic response of the LSV has been quantitatively assessed at multiple sites using GIT, we evaluated the effectiveness of the 3D model by attempting to reproduce the observed amplification functions through site-to-site transfer functions derived from the model.

Laurenzano et al. [22] obtained an estimation of the frequency

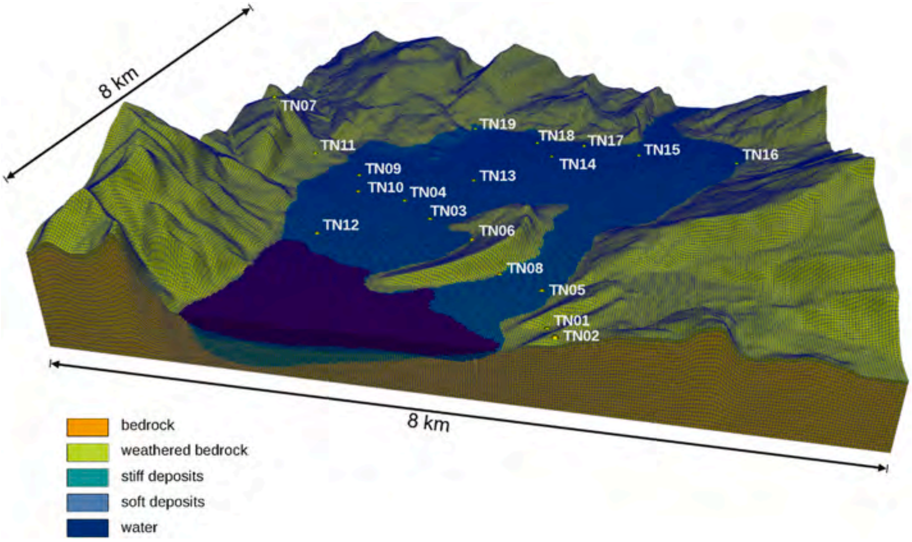

Fig. 12. View of the central part of the discretised spatial domain used in numerical simulations with the spectral elements method. The grid cells correspond to the spectral elements and their colour corresponds to the structural unit to which the element is assigned, with the physical properties given in Table (1). For computational efficiency (see Section 3.4), the water structural unit was assigned the same elastic properties as the soft sedimentary deposits. The locations of the seismic stations are also marked within the domain. (For interpretation of the references to colour in this figure legend, the reader is referred to the Web version of this article.)

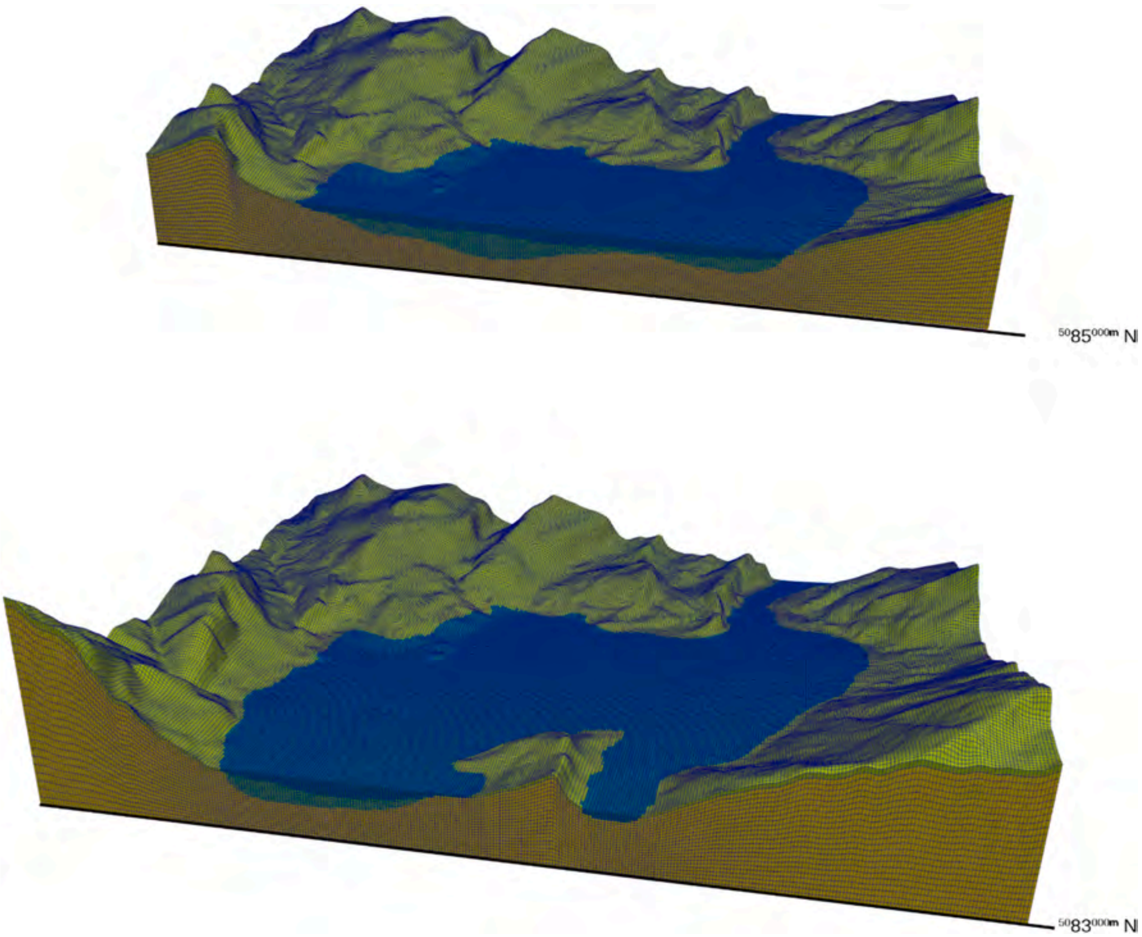

Fig. 13. Two clipped views of the discretised spatial domain with vertical cut along the latitudes 5385000 and 538300 m North, respectively. See Fig. 12 for the color legend. (For interpretation of the references to colour in this figure legend, the reader is referred to the Web version of this article.)

amplification function for the horizontal components at 18 sites in the LSV in respect to a reference site denoted TN02, which is characterized by a Vs_{30} of about 1000 m/s (the locations of the 19 stations are mapped in Fig. 3). This estimation was obtained by applying the one–step generalized inversion [75] implemented in an improved version of the GITANES (GIT ANalysis of Earthquake Spectra) package [76,77] to a dataset of weak motion recordings of 93 local and regional events collected between the years 2019 and 2021. To validate the applicability of the 3D model for physics-based numerical simulations of ground motion, we compare the spectral amplification empirically determined by Laurenzano et al. [22] with the spectral amplification obtained from the numerically evaluated site-to-site transfer function $\mathbf{T}(\boldsymbol{x}, \boldsymbol{x_0}, f)$, with $\boldsymbol{x_0}$ corresponding to the location of station TN02. In order to evaluate the amplification from $\mathbf{T}(\boldsymbol{x}, \boldsymbol{x_0}, f)$, we can follow Borcherdt [78] and consider the spectral amplification $A(\boldsymbol{x}, \boldsymbol{x_0}, f)$ as the expected value of the ratio between the amplitude spectrum of the horizontal ground motion at the observation site $\boldsymbol{x}$ and that in a reference site $\boldsymbol{x_0}$. We define here the amplitude spectrum of the horizontal ground motion as the geometrical mean of the Fourier Amplitude Spectra(FAS) of the two horizontal components $u_1(\boldsymbol{x},t)$ and $u_2(\boldsymbol{x},t)$. If we denote with E the expected value operator, we can write

$$A(\boldsymbol{x},\boldsymbol{x_0},f) = E\left[\frac{(|F[u_1(\boldsymbol{x},t)]|\cdot|F[u_2(\boldsymbol{x},t)]|)^{\frac{1}{2}}}{(|F[u_1(\boldsymbol{x_0},t)]|\cdot|F[u_2(\boldsymbol{x_0},t)]|)^{\frac{1}{2}}}\right]. \tag{4}$$

If we assign to the reference site $\boldsymbol{x_0}$ a population of three-component earthquake records, we can express the spectral amplification at a generic site $\boldsymbol{x}$ in respect to the site $\boldsymbol{x_0}$ by substituting Eq. (2) into Eq. (4) and obtaining

$$A(\boldsymbol{x},\boldsymbol{x_0},f) = E\left[\frac{\left(\left|\sum_{j=1}^{3} T_{1j}(\boldsymbol{x},\boldsymbol{x_0},f)F\left[u_j(\boldsymbol{x_0},t)\right]\right|\cdot\left|\sum_{j=1}^{3} T_{2j}(\boldsymbol{x},\boldsymbol{x_0},f)F\left[u_j(\boldsymbol{x_0},t)\right]\right|\right)^{\frac{1}{2}}}{(|F[u_1(\boldsymbol{x_0},t)]|\cdot|F[u_2(\boldsymbol{x_0},t)]|)^{\frac{1}{2}}}\right]. \tag{5}$$

We considered as $\boldsymbol{u}(\boldsymbol{x_0},t)$ the three-component recording of each of the 93 seismic events collected in the station located in the chosen reference site TN02 and used the geometrical mean as the expectation value for the estimation of $A(\boldsymbol{x}, \boldsymbol{x_0}, f)$ as in Eq. (5) for the remaining 18 stations. In Fig. 14 we plot the amplification functions resulting from the 3D model along with the empirical amplification functions by adding, for comparison, the amplitude of the linear frequency-domain transfer function for the 1D Vs profile extracted from the 3D model under each station. The transfer function for the 1D profile was evaluated using the SeismoSoil code [79].

When comparing the amplification functions obtained through the 3D or 1D approaches with the empirical ones, it is important to keep in mind that the latter are inherently affected by a degree of uncertainty. This uncertainty can be quantified by the standard error resulting from the generalized inversion method used in their evaluation. To assess the discrepancy between the modeled and empirical curves in light of this uncertainty, we adopted a frequency-averaged logarithmic misfit, normalized by the corresponding standard error.

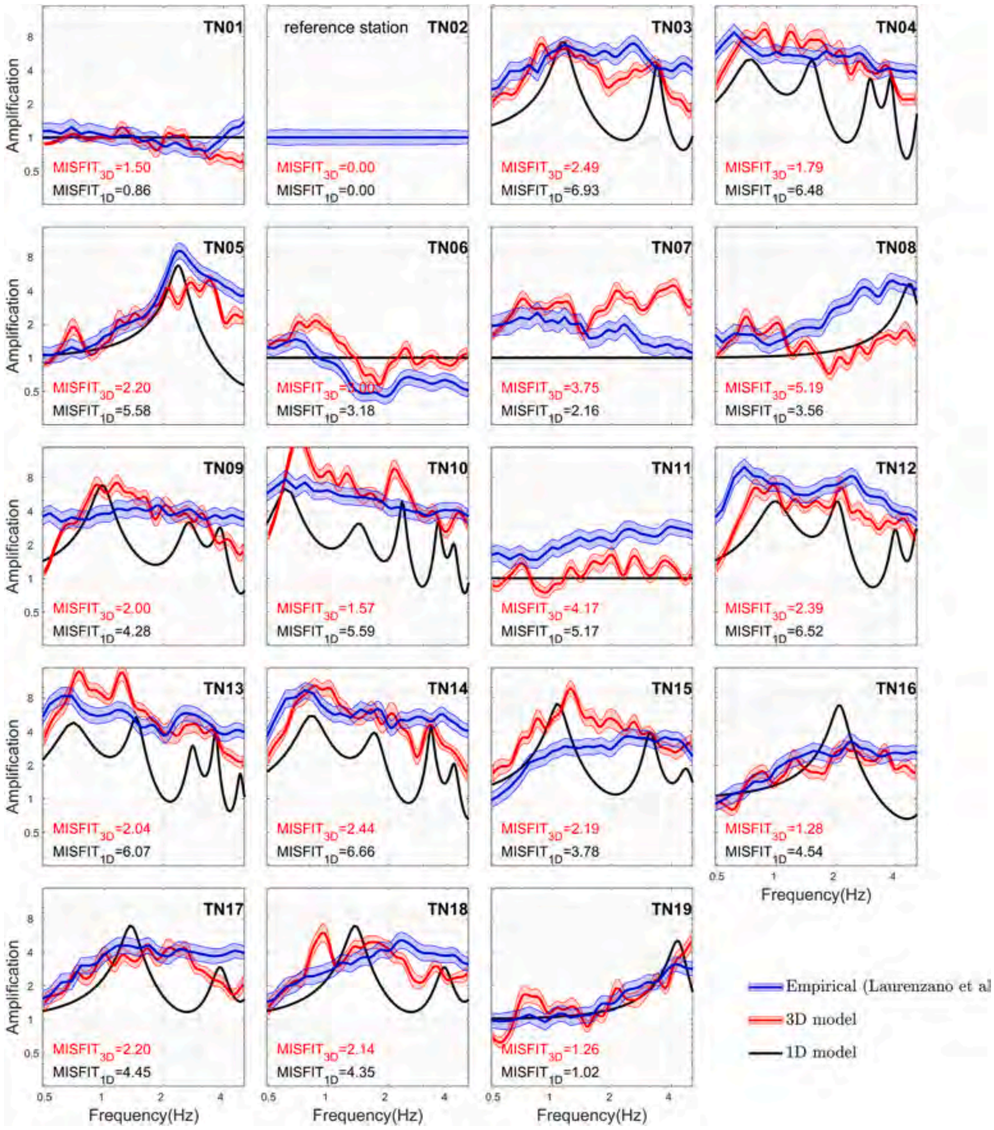

Fig. 14. Station by station (see map in Fig. 3) comparison of the empirical amplification function obtained in Laurenzano et al. [22] (in blue) with the amplification function estimated with 3D numerical simulations (in red) and with the 1D amplification function resulting from the vertical Vs profile extracted from the 3D geomodel below each station (in black). All the amplification curves refer to the same reference station TN02. The misfit between the simulated and empirical curves is estimated according to eq. (6). (For interpretation of the references to colour in this figure legend, the reader is referred to the Web version of this article.)

$$m = \frac{1}{f_2 - f_1} \int_{f_1}^{f_2} \frac{|\ \ln A^{(test)} - \ln A^{(target)}|}{SE_{ln}^{(target)}} df \qquad (6)$$

In equation (6) $A^{(test)}$ and $A^{(target)}$are the test and target amplification functions, respectively, f_1 and f_2 are the extremes of the frequency range and $SE_{ln}^{(target)}$ is the standard error of the logarithm of the target amplification function. A desirable fit would require a m value of the order of unity or less.

We can see an overall good agreement between the empirical amplification functions (in blue) and the predicted amplification functions obtained using 3D transfer functions (in red), even if the fit still leaves some room for improvement. We can observe that the 3D simulations for the stations in the center of the valley predict broadband amplifications with values of up to 8, whose shape almost matches that of the empirical curves, while the amplification functions predicted from the 1D Vs profile (in black), only reach these values for isolated peaks. In the same figure, the semi-transparent bands enclosing the empirical and 3D model amplification curves describe the standard error associated with the generalized inversion and the standard deviation associated with the assessment of the expectation value of the synthetic amplification (Eq. (5)), respectively.

The misfit values associated with the amplification functions computed from the 3D model are systematically lower than those from the 1D model, with two notable exceptions: station TN08, where the 3D model yields a significantly larger misfit, and stations located on rock sites (TN01, TN06, TN07, TN11), where the misfits from both models are comparable. While the misfit at station TN01 is relatively small, the discrepancies observed at the other rock stations indicate that the assumption of bedrock homogeneity in the 3D model may not be fully justified. To enhance the model's accuracy, it would be beneficial to collect additional data on the subsurface physical properties at these locations. In contrast, the misfit observed at station TN08 may be due to its transitional position between soil and rock beneath Monte Brione, which appears to require a more refined resolution in the model.

From the amplitude spectra of the numerical $\mathbf{T}(\boldsymbol{x}, \boldsymbol{x}_0, f)$ at two stations, one located on a rock site and the other on a soft soil site (Fig. 15) it is evident that the station located on soft soil exhibits pronounced peaks not only in the diagonal but also in the off-diagonal components. This indicates that the constructed 3D model captures cross-coupling

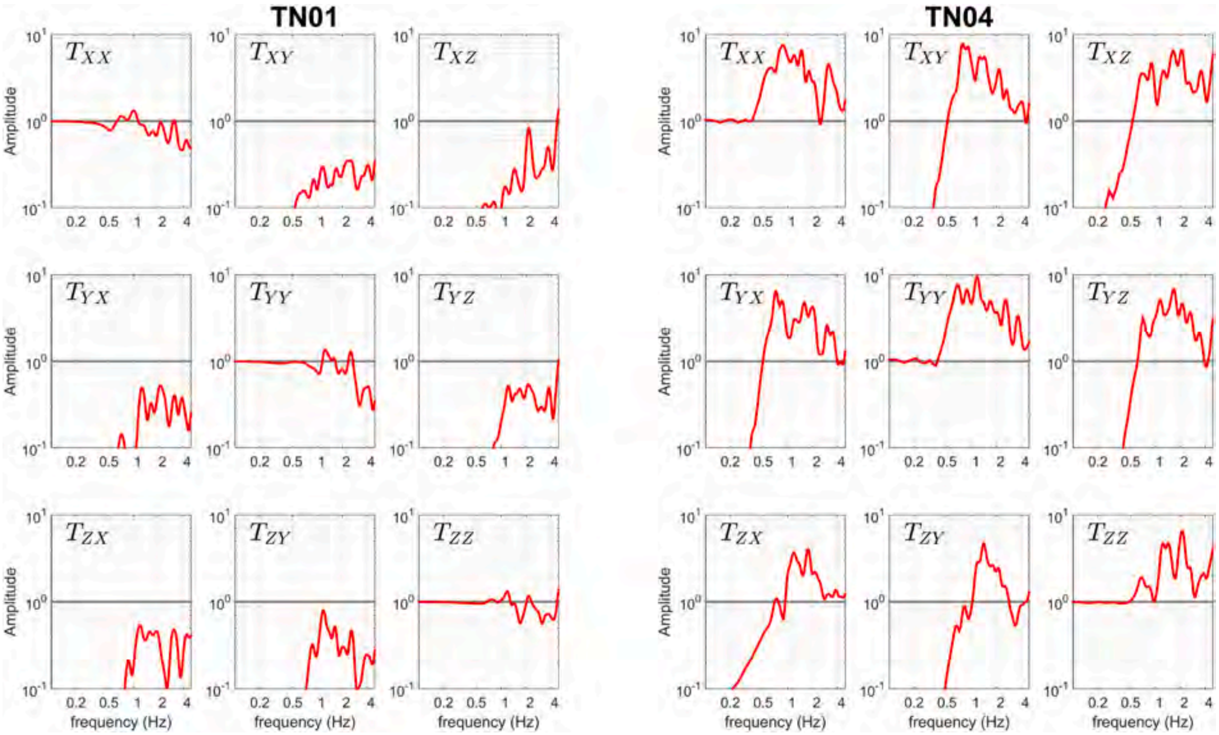

Fig. 15. The amplitude spectra of the 9 components of the site-to-site transfer functions evaluated from numerical simulations in the locations of the temporary stations TN01 (a rock site) and TN04 (a soft soil site), in relation to the reference site TN02.

effects, consistent with the findings reported by Parolai et al. [23].

Figs. 16 and 17 present two examples comparing predicted and recorded three-component waveforms for two magnitude 3.6 events at short and intermediate distance, respectively. In addition to visual inspection, we evaluate the discrepancies in peak ground velocity and acceleration using the Goodness-of-Fit scores S_{pgv} and S_{pga}, as defined by Anderson[80]. In order to have an overview of the model capability to predict the observed waveforms, in Fig. 18 we plot the average S_{pgv} across 19 temporary stations, based on a dataset of 90 seismic events.

In the first example (Fig. 16), we compare recorded and simulated waveforms at the rock site TN01 and the soil site TN10 for a M 3.6 event at hypocentral distance of about 20 km from the reference station TN02. The model performs well at TN01, accurately reproducing the observed amplitudes. However, at TN10, the predicted amplitudes are overestimated. In the second example (Fig. 17), we examine signals from the rock site TN06 and the soil site TN04 for a M 3.6 event at hypocentral distance of about 144 km. The model slightly overestimates ground motion at TN06, while the prediction at TN04 aligns closely with the recorded data.

Fig. 18 provides further insight into the predictive performance of the model, reaffirming some of the previously noted limitations at station TN08. It also suggests that the model's performance at the rock sites TN06, TN07, and TN11 could be improved. Additionally, the figure draws attention to a potential issue at the soil site TN10. Interestingly, this occurs despite TN10's amplification function showing a relatively low misfit when compared with the observed amplification (see Fig. 14), indicating that further investigation may be warranted. Overall, the model performs well at most stations, with more than half achieving an average Anderson's score above 8.

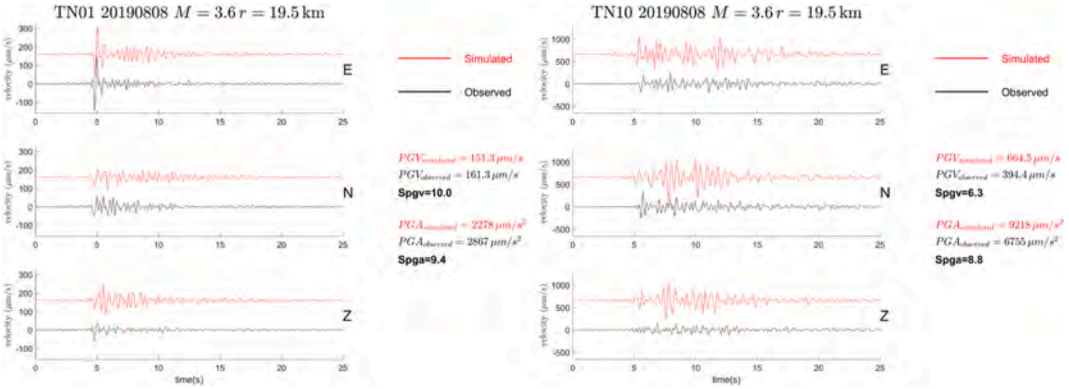

Fig. 16. Observed vs. Simulated Waveforms: Waveform comparison at a rock site (TN01, left) and a soil site (TN10, right), showing observed (black) and simulated (red) traces. The event occurred at an intermediate hypocentral distance of 19.5 km from reference station TN02. Goodness-of-fit scores are reported using Spgv and Spga metrics, as defined by Anderson [80]. (For interpretation of the references to colour in this figure legend, the reader is referred to the Web version of this article.)

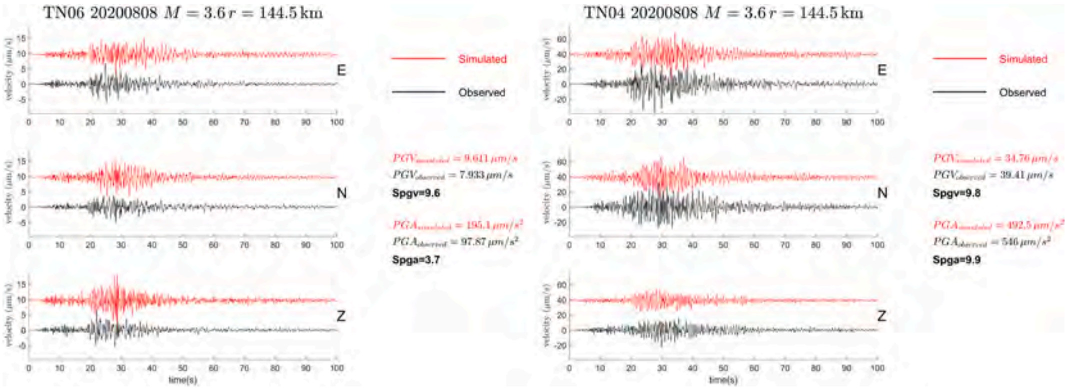

Fig. 17. Observed vs. Simulated Waveforms: Waveform comparison at a rock site (TN06, left) and a soil site (TN04, right), showing observed (black) and simulated (red) traces. The event occurred at an intermediate hypocentral distance of 144.5 km from reference station TN02. Goodness-of-fit scores are reported using Spgv and Spga metrics, as defined by Anderson [80]. (For interpretation of the references to colour in this figure legend, the reader is referred to the Web version of this article.)

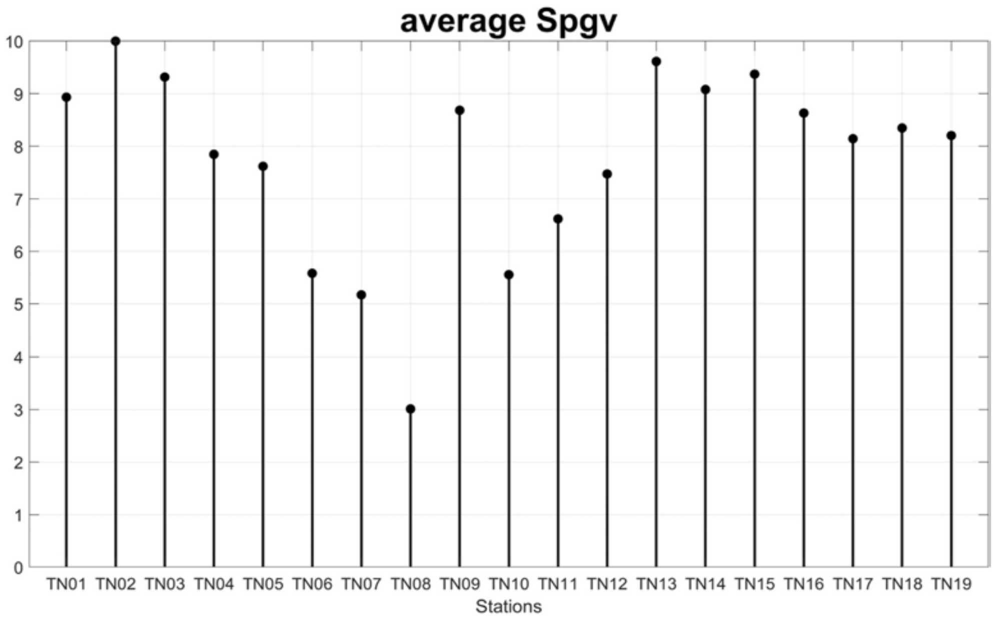

Fig. 18. Average Goodness-of-Fit Score for Peak Ground Velocity: Comparison between simulated and observed 3-component waveforms across 19 temporary stations, based on a dataset of 90 seismic events.

5. Conclusions

We built a 3D model of the subsoil of the alpine valley on the northern shore of Lake Garda (Italy) to explain the origin of the site effects in the valley and to provide reliable ground motion predictions using physics-based numerical simulations. The 3D model was obtained by combining geological and geophysical data from published studies as well as from unpublished results of recent surveys. In particular, we used the indirect measurement of the S-wave velocity in the shallow layers resulting from MASW and the indirect measurement of the sediment thickness resulting from the peak frequency in microtremor HVSR, after having determined the relationship between sediment thickness and peak frequency. Gravimetric methods were applied to refine the understanding of the buried valley's geometry and to identify lateral density variations that characterize its internal structure.

An important part of the present work was to evaluate the agreement of the obtained 3D model with the observed seismic response of the valley up to a frequency of 5 Hz. To this aim, we carried out the numerical calculation of seismic wave propagation for vertically incident plane waves, using high performance software SPECFEM3D [27], which is based on the spectral elements method. In this way we evaluated 9-component 3D site-to-site transfer functions for a selected reference site. With the 3D site-to-site transfer function, it is possible to predict the three-component ground motion at the points of the spatial domain from the input motion associated with the reference site by considering the possible cross-coupling effects between the ground motion components, whose presence in LSV was demonstrated in a previous study.

We tested the constructed 3D model by comparing the spectral amplification functions (AF) that were obtained in a previous study [22] at 19 temporary stations with the amplification curves resulting from the application of the numerically evaluated 3D site-to-site transfer function at the same stations (synthetic 3D AF). We repeated the comparison with the synthetic 1D AF derived from the shear wave velocity vertical profile that was extracted from the 3D model under each station. In most cases, the agreement between synthetic 3D AF and empirical AF was better than that of synthetic 1D AF, suggesting that lateral heterogeneities in the subsurface significantly influence local seismic site effects in the studied valley.

The comparison between predicted and observed amplification functions provides encouraging insights into the potential of the 3D model for simulating seismic scenarios. However, a definitive assessment of its applicability requires further validation. In an upcoming study, we plan to use the current model to reproduce recorded ground motions from several local earthquakes, thereby significantly extending the spatial domain. This approach will allow a more comprehensive evaluation of the LSV model's predictive capabilities.

The constructed 3D model was intended for simulating earthquake scenarios within the frequency range up to 5 Hz. However, excluding ground motion components above 5 Hz may lead to an underestimation of seismic demand—particularly in terms of peak ground acceleration (PGA). To address this limitation the evaluated scenarios should eventually be supplemented with a stochastic high-frequency extension, following one of the hybrid approaches proposed in literature ([81]; e. g. Ref. [82]), which are designed to overcome the high-frequency constraints of physics-based ground motion simulations. On the other hand, the current 3D model could represent a valuable starting point for developing a more refined model capable of realistically predicting seismic response in the lower Sarca Valley across the broader frequency spectrum.

CRediT authorship contribution statement

Peter Klin: Writing – original draft, Visualization, Software, Investigation. **Ilaria Primofiore:** Visualization, Investigation. **Luigi Zampa:** Writing – original draft, Visualization, Investigation. **Marco Garbin:** Visualization, Investigation, Data curation. **Alfio Viganò:** Writing – original draft, Visualization. **Francesco Palmieri:** Resources, Investigation, Data curation. **Carla Barnaba:** Writing – original draft, Investigation, Data curation. **Stefano Parolai:** Supervision. **Giovanna Laurenzano:** Writing – original draft, Supervision, Project administration, Data curation, Conceptualization.

Declaration of competing interest

The authors declare that they have no known competing financial interests or personal relationships that could have appeared to influence the work reported in this paper.

Acknowledgments

We acknowledge the CINECA award under the ISCRA initiative, for the availability of high performance computing resources and support.

We thank Dr. T. Garbari and Dr. L. Veronese for providing the results of the ATM Magnetotelluric survey. We thank Prof. A. Marzocchi for providing the bathymetry of the Lake Garda.

Maps in this work were generated using the Generic Mapping Tools (GMT) version 6.0 [83].

Finally, we extend our sincere thanks to reviewer Filippo Gatti, the two anonymous reviewers, and the editor for their constructive feedback, which significantly contributed to enhancing the quality of our manuscript.

This work was carried out within the project "Studio riguardante la risposta sismica locale del tratto terminale della valle del fiume Sarca in prossimità del Lago di Garda", funded by the Provincia Autonoma di Trento and was part of the Multi-annual Research Program for the XV Legislative Term of the Provincia Autonoma di Trento, approved by Provincial Government Resolution No. 1229 of July 20, 2015.

Part of this study was carried out within the RETURN Extended Partnership and received funding from the European Union Next-GenerationEU (National Recovery and Resilience Plan – NRRP, Mission 4, Component 2, Investment 1.3 – D.D. 1243 August 2, 2022, PE0000005).

Appendix A. reference-to-site transfer function for vertically incident plane waves

In Section 4, we attempt a validation of the 3D model of the LSV using a site-to-site transfer function, that allows the three-component seismic response $\boldsymbol{u}(\boldsymbol{x},t)$ to a vertically incident wave motion at a generic observation point $\boldsymbol{x}$, to be expressed in terms of the response $\boldsymbol{u}(\boldsymbol{x}_0,t)$ at the reference site $\boldsymbol{x}_0$. We can deduce the existence of such a function from the existence of the site-specific impulsive responses to a vertically emerging plane wave. If we denote with $H_{ij}(\boldsymbol{x},f)$ the complex Fourier spectrum of the i-th spatial component of the response at location $\boldsymbol{x}$ corresponding to a vertically incident impulsive plane wave polarized in the j-th spatial direction, we can express the response to an incoming vertically incident three-component input motion having Fourier spectrum $\boldsymbol{U}^{INP}(f)$

$$U_i(x,f) = \sum_{j=1}^{3} H_{ij}(x,f) U_j^{INP}(f) \tag{A.1}$$

or

$$\boldsymbol{U}(\boldsymbol{x},f) = \mathbf{H}(\boldsymbol{x},f)\ \boldsymbol{U}^{INP}(f) \tag{A.2}$$

in matrix notation (with bold italic denoting 3 component column vectors and bold roman denoting 3x3 matrices). If the reference site $\boldsymbol{x}_0$ is close enough to the observation site $\boldsymbol{x}$ so that we can assume that both are affected by the same input motion $\boldsymbol{U}^{INP}(f)$, as in Fig. 9, we can also write

$$\boldsymbol{U}(\boldsymbol{x}_0,f) = \mathbf{H}(\boldsymbol{x}_0,f)\ \boldsymbol{U}^{INP}(f) \tag{A.3}$$

The requirement for an ideal reference site would correspond to $\mathbf{H}(\boldsymbol{x}_0,f) = 2\mathbf{I}$, with $\mathbf{I}$ the identity matrix. In our construction we can relax this unrealistic requirement to a much less restrictive condition that $\mathbf{H}(\boldsymbol{x}_0,f)$ is invertible (i.e. $\det(\mathbf{H}(\boldsymbol{x}_0,f)) \neq 0$). If that condition is verified, we can express

$$\boldsymbol{U}^{INP}(f) = \mathbf{H}^{-1}(\boldsymbol{x}_0,f)\ \boldsymbol{U}(\boldsymbol{x}_0,f) \tag{A.4}$$

and substituting eq. (A4) in eq. (A2) we can describe the three component motion $\boldsymbol{U}(\boldsymbol{x},f)$ in the observation point $\boldsymbol{x}$ in terms of the three component motion $\boldsymbol{U}(\boldsymbol{x}_0,f)$ at the reference site $\boldsymbol{x}_0$, when both sites are affected by the same incoming vertically incident input motion. We can write

$$\boldsymbol{U}(\boldsymbol{x},f) = \mathbf{T}(\boldsymbol{x},\boldsymbol{x}_0,f)\ \boldsymbol{U}(\boldsymbol{x}_0,f), \tag{A.5}$$

where we have introduced the site-to-site 9-component transfer function as

$$\mathbf{T}(\boldsymbol{x}, \boldsymbol{x}_0, f) = \mathbf{H}(\boldsymbol{x}, f)\ \mathbf{H}^{-1}(\boldsymbol{x}_0, f). \tag{A.6}$$

In the following we show how can we practically evaluate the site-to-site transfer function $\mathbf{T}(\boldsymbol{x}_0, \boldsymbol{x}, f)$ with numerical modeling of seismic waves on the basis of the 3D viscoelastic model of the subsoil. The approach consists in the numerical evaluation of the three different solutions $\boldsymbol{U}^{(X)}(\boldsymbol{x},f)$, $\boldsymbol{U}^{(Y)}(\boldsymbol{x},f)$ and $\boldsymbol{U}^{(Z)}(\boldsymbol{x},f)$ corresponding to the three input motions

$$\begin{aligned} \boldsymbol{X}^{INP}(f) &= [S(f), 0, 0]^T, \\ \boldsymbol{Y}^{INP}(f) &= [0, S(f), 0]^T, \\ \boldsymbol{Z}^{INP}(f) &= [0, 0, S(f)\ ]^T, \end{aligned} \tag{A.7}$$

respectively, where the notation $[\text{-},\text{-},\text{-}]^{\mathrm{T}}$ denotes a 3-component column vector and where $S(f)$ is the scalar complex Fourier spectrum of a broadband signal or pseudo-impulse, used in the numerical modelling as the signature of the incoming polarized plane wave. The only requirement for $S(f)$ consists in having non-negligible value of the modulus all over the frequency band of interest and in being compatible with the adopted numerical modelling scheme. According to Eq. (A2) the computed solutions in the generic site would correspond to

$$\begin{aligned} \boldsymbol{U}^{(X)}(\boldsymbol{x},f) &= S(f)[H_{11}(\boldsymbol{x},f), H_{12}(\boldsymbol{x},f), H_{13}(\boldsymbol{x},f)]^T, \\ \boldsymbol{U}^{(Y)}(\boldsymbol{x},f) &= S(f)[H_{21}(\boldsymbol{x},f), H_{22}(\boldsymbol{x},f), H_{23}(\boldsymbol{x},f)]^T, \\ \boldsymbol{U}^{(Z)}(\boldsymbol{x},f) &= S(f)[H_{31}(\boldsymbol{x},f), H_{32}(\boldsymbol{x},f), H_{33}(\boldsymbol{x},f)\ ]^T, \end{aligned} \tag{A.8}$$

and we can express the components of the response function in the generic observation site in terms of the three numerical solutions as

$$\mathbf{H}(\boldsymbol{x},f) = \frac{1}{S(f)} \begin{bmatrix} U_1^{(X)}(\boldsymbol{x},f) & U_1^{(Y)}(\boldsymbol{x},f) & U_1^{(Z)}(\boldsymbol{x},f) \\ U_2^{(X)}(\boldsymbol{x},f) & U_2^{(Y)}(\boldsymbol{x},f) & U_2^{(Z)}(\boldsymbol{x},f) \\ U_3^{(X)}(\boldsymbol{x},f) & U_3^{(Y)}(\boldsymbol{x},f) & U_3^{(Z)}(\boldsymbol{x},f) \end{bmatrix} \tag{A.9}$$

Once verified that $\mathbf{H}(\boldsymbol{x}_0,f)$ is invertible for each frequency in the frequency band of interest, we can apply eq. (A6) and compute

$$\mathbf{T}(\boldsymbol{x}, \boldsymbol{x}_0, f) = \begin{bmatrix} U_1^{(X)}(\boldsymbol{x},f) & U_1^{(Y)}(\boldsymbol{x},f) & U_1^{(Z)}(\boldsymbol{x},f) \\ U_2^{(X)}(\boldsymbol{x},f) & U_2^{(Y)}(\boldsymbol{x},f) & U_2^{(Z)}(\boldsymbol{x},f) \\ U_3^{(X)}(\boldsymbol{x},f) & U_3^{(Y)}(\boldsymbol{x},f) & U_3^{(Z)}(\boldsymbol{x},f) \end{bmatrix} \begin{bmatrix} U_1^{(X)}(\boldsymbol{x}_0,f) & U_1^{(Y)}(\boldsymbol{x}_0,f) & U_1^{(Z)}(\boldsymbol{x}_0,f) \\ U_2^{(X)}(\boldsymbol{x}_0,f) & U_2^{(Y)}(\boldsymbol{x}_0,f) & U_2^{(Z)}(\boldsymbol{x}_0,f) \\ U_3^{(X)}(\boldsymbol{x}_0,f) & U_3^{(Y)}(\boldsymbol{x}_0,f) & U_3^{(Z)}(\boldsymbol{x}_0,f) \end{bmatrix}^{-1} \quad (A.10) \tag{A.10}$$

by means of standard algebraic rules.

Data availability

Data will be made available on request.

References

[1] Gutenberg B. Effects of ground on earthquake motion. Bull Seismol Soc Am 1957;47(3):221–50. https://doi.org/10.1785/BSSA0470030221.

[2] Haskell NA. Crustal reflection of plane SH waves. J Geophys Res 1960;65(12):4147–50. https://doi.org/10.1029/JZ065i012p04147. 1896-1977.

[3] Bard P.-Y., Bouchon M. The two-dimensional resonance of sediment-filled valleys. Bull Seismol Soc Am 1985;75(2):519–541.https://pubs.geoscienceworld.org/ssa/bssa/article-abstract/75/2/519/118695/The-two-dimensional-resonance-of-sediment-filled.

[4] Koketsu K, Kikuchi M. Propagation of seismic ground motion in the Kanto basin, Japan. Science 2000;288(5469):1237–9. https://doi.org/10.1126/science.288.5469.1237.

[5] Pilz M, Parolai S, Petrovic B, Silacheva N, Abakanov T, Orunbaev S, Moldobekov B. Basin-edge generated rayleigh waves in the Almaty basin and corresponding consequences for ground motion amplification. Geophys J Int 2018;213(1):301–16. https://doi.org/10.1093/gji/ggx555.

[6] Di Giulio G, Rovelli A, Cara F, Azzara RM, Marra F, Basili R, Caserta A. Long-duration asynchronous ground motions in the Colfiorito plain, central Italy, observed on a two-dimensional dense array. J Geophys Res Solid Earth 2003;108(B10). https://doi.org/10.1029/2002JB002367.

[7] Pacor F, Bindi D, Luzi L, Parolai S, Marzorati S, Monachesi G. Characteristics of strong ground motion data recorded in the Gubbio sedimentary basin (central Italy). Bull Earthq Eng 2007;5(1):27–43. https://doi.org/10.1007/s10518-006-9026-x.

[8] Bindi D, Parolai S, Cara F, Di Giulio G, Ferretti G, Luzi L, Monachesi G, Pacor F, Rovelli A. Site amplifications observed in the Gubbio basin, central Italy: hints for lateral propagation effects. Bull Seismol Soc Am 2009;99(2A):741–60. https://doi.org/10.1785/0120080238.

[9] Bindi D, Luzi L, Parolai S, Di Giacomo D, Monachesi G. Site effects observed in alluvial basins: the case of Norcia (central Italy). Bull Earthq Eng 2011;9(6):1941–59. https://doi.org/10.1007/s10518-011-9273-3.

[10] Barnaba C, Marello L, Vuan A, Palmieri F, Romanelli M, Priolo E, Braitenberg C. The buried shape of an alpine valley from gravity surveys, seismic and ambient noise analysis. Geophys J Int 2010;180(2):715–33. https://doi.org/10.1111/j.1365-246X.2009.04428.x.

[11] Kawase H. The cause of the damage belt in kobe: “the Basin-Edge Effect,” constructive interference of the direct S-Wave with the basin-induced diffracted/rayleigh waves. Seismol Res Lett 1996;67(5):25–34. https://doi.org/10.1785/gssrl.67.5.25.

[12] Roten D, Fäh D, Olsen KB, Giardini D. A comparison of observed and simulated site response in the Rhône valley. Geophys J Int 2008;173(3):958–78. https://doi.org/10.1111/j.1365-246X.2008.03774.x.

[13] Maufroy E, et al. Earthquake ground motion in the mygdonian basin, Greece: the E2VP verification and validation of 3D numerical simulation up to 4 Hz. Bull Seismol Soc Am 2015;105(3):1398–418. https://doi.org/10.1785/0120140228.

[14] Cruz-Atienza VM, Tago J, Sanabria-Gómez JD, Chaljub E, Etienne V, Virieux J, Quintanar L. Long duration of ground motion in the paradigmatic valley of Mexico, 1. Sci Rep 2016;6(1):38807. https://doi.org/10.1038/srep38807.

[15] Thompson M, Wirth EA, Frankel AD, Renate Hartog J, Vidale JE. Basin amplification effects in the Puget lowland, Washington, from strong-motion recordings and 3D simulations. Bull Seismol Soc Am 2020;110(2):534–55. https://doi.org/10.1785/0120190211.

[16] Hu Z, Olsen KB, Day SM. 0–5 Hz deterministic 3-D ground motion simulations for the 2014 La Habra, California, Earthquake. Geophys J Int 2022;230(3):2162–82. https://doi.org/10.1093/gji/ggac174.

[17] Castro-Cruz D, Gatti F, Lopez-Caballero F, Hollender F, El Haber E, Causse M. Blind broad-band (0–10 hz) numerical prediction of the 3-D near field seismic response of an MW6.0 extended fault scenario: application to the nuclear site of Cadarache (France). Geophys J Int 2023;232(1):581–600. https://doi.org/10.1093/gji/ggac346.

[18] Callaghan S, et al. Using open-science workflow tools to produce SCEC CyberShake physics-based probabilistic seismic hazard models. Front High Perform Comput 2024;2. https://doi.org/10.3389/fhpcp.2024.1360720.

[19] Klin P, Laurenzano G, Romano MA, Priolo E, Martelli L. ER3D: a structural and geophysical 3-D model of central Emilia-Romagna (northern Italy) for numerical simulation of earthquake ground motion. Solid Earth 2019;10(3):931–49. https://doi.org/10.5194/se-10-931-2019.

[20] Panzera F, Alber J, Imperatori W, Bergamo P, Fäh D. Reconstructing a 3D model from geophysical data for local amplification modelling: the study case of the

upper Rhone valley, Switzerland. Soil Dynam Earthq Eng 2022;155:107163. https://doi.org/10.1016/j.soildyn.2022.107163.

[21] Stucchi M, Meletti C, Montaldo V, Crowley H, Calvi GM, Boschi E. Seismic hazard assessment (2003–2009) for the Italian building code. Bull Seismol Soc Am 2011; 101(4):1885–911. https://doi.org/10.1785/0120100130.

[22] Laurenzano G, Garbin M, Parolai S, Barnaba C, Romanelli M, Froner L. High-resolution local seismic zonation by cluster and correlation analysis. Soil Dynam Earthq Eng 2023;173:108122. https://doi.org/10.1016/j.soildyn.2023.108122.

[23] Parolai S, Laurenzano G, Garbin M. Estimating cross-coupling in site response by seismic noise interferometry: an example from an alpine valley (Northeastern Italy). Seismol Res Lett 2022;94(1):140–8. https://doi.org/10.1785/0220220099.

[24] Paolucci R. Numerical evaluation of the effect of cross-coupling of different components of ground motion in site response analyses. Bull Seismol Soc Am 1999; 89(4):877–87. https://doi.org/10.1785/BSSA0890040877.

[25] Calcagno P, Chilès JP, Courrioux G, Guillen A. Geological modelling from field data and geological knowledge: part I. Modelling method coupling 3D potential-field interpolation and geological rules. Phys Earth Planet Inter 2008;171(1):147–57. https://doi.org/10.1016/j.pepi.2008.06.013.

[26] Tong P, Chen C, Komatitsch D, Basini P, Liu Q. High-resolution seismic array imaging based on an SEM-FK hybrid method. Geophys J Int 2014;197(1):369–95. https://doi.org/10.1093/gji/ggt508.

[27] Peter D, et al. Forward and adjoint simulations of seismic wave propagation on fully unstructured hexahedral meshes. Geophys J Int 2011;186(2):721–39. https://doi.org/10.1111/j.1365-246X.2011.05044.x.

[28] Zhu C, Cotton F, Kwak D-Y, Ji K, Kawase H, Pilz M. Within-site variability in earthquake site response. Geophys J Int 2022;229(2):1268–81. https://doi.org/10.1093/gji/ggab481.

[29] Thompson EM, Baise LG, Tanaka Y, Kayen RE. A taxonomy of site response complexity. Soil Dynam Earthq Eng 2012;41:32–43. https://doi.org/10.1016/j.soildyn.2012.04.005.

[30] Maufroy E, Chaljub E, Theodoulidis NP, Roumelioti Z, Hollender F, Bard P, de Martin F, Guyonnet-Benaize C, Margerin L. Source-related variability of site response in the Mygdonian basin (Greece) from accelerometric recordings and 3D numerical simulations. Bull Seismol Soc Am 2017;107(2):787–808. https://doi.org/10.1785/0120160107.

[31] Castellarin A, et al. Note Illustrative della Carta geologica d'Italia alla scala 1: 50.000, F. 080 Riva del Garda. Servizio Geologico d'Italia - ISPRA; 2005.

[32] Castellarin A, Vai GB, Cantelli L. The alpine evolution of the Southern Alps around the Giudicarie faults: a Late Cretaceous to early Eocene transfer zone. Tectonophysics 2006;414(1):203–23. https://doi.org/10.1016/j.tecto.2005.10.019.

[33] Picotti V, Prosser G, Castellarin A. Structures and kinematics of the Giudicarie-Val Trompia fold and thrust belt (Central Southern Alps, Northern Italy). Mem Sci Geol 1995;47:95–109.

[34] Felber M, Veronese L, Cocco L, Frei W, Nardin M, Oppizzi P, Santuliana E, Violanti D. Indagini sismiche e geognostiche nelle valli del Trentino meridionale (Val d'Adige, Valsugana, Valle del Sarca, Valle del Chiese), Italia. Studi Trentini Sci Nat Acta Geol 2000;75:3–52.

[35] Ravazzi C, Pini R, Badino F, De Amicis M, Londeix L, Reimer PJ. The latest LGM culmination of the Garda glacier (Italian Alps) and the onset of glacial termination. Age of glacial collapse and vegetation chronosequence. Quat Sci Rev 2014;105: 26–47. https://doi.org/10.1016/j.quascirev.2014.09.014.

[36] Viganò A, Scafidi D, Martin S, Spallarossa D. Structure and properties of the Adriatic crust in the Central-Eastern Southern Alps (Italy) from local earthquake tomography. Terra Nova 2013;25(6):504–12. https://doi.org/10.1111/ter.12067.

[37] Guidoboni E, Ferrari G, Mariotti D, Comastri A, Tarabusi G, Sgattoni G, Valensise G. CFTI5Med Catalogo dei Forti Terremoti in Italia (461 a.C.-1997) e nell'area Mediterranea (760 a.C.-1500). Istituto Nazionale di Geofisica e Vulcanologia (INGV) 2018. https://doi.org/10.6092/ingv.it-cfti5.

[38] Viganò A, Scafidi D, Ranalli G, Martin S, Della Vedova B, Spallarossa D. Earthquake relocations, crustal rheology, and active deformation in the Central–Eastern Alps (N Italy). Tectonophysics 2015;661:81–98. https://doi.org/10.1016/j.tecto.2015.08.017.

[39] Viganò A, Bressan G, Ranalli G, Martin S. Focal mechanism inversion in the Giudicarie–Lessini seismotectonic region (Southern Alps, Italy): insights on tectonic stress and strain. Tectonophysics 2008;460(1):106–15. https://doi.org/10.1016/j.tecto.2008.07.008.

[40] Viganò A, Scafidi D, Ferretti G. A new approach for a fully automated earthquake monitoring: the local seismic network of the Trentino region (NE Italy). J Seismol 2021;25(2):419–32. https://doi.org/10.1007/s10950-021-09993-0.

[41] Lajaunie C, Courrioux G, Manuel L. Foliation fields and 3D cartography in geology: principles of a method based on potential interpolation. Math Geol 1997;29(4): 571–84. https://doi.org/10.1007/BF02775087.

[42] Tarquini S, Isola I, Favalli M, Mazzarini F, Bisson M, Pareschi MT, Boschi E. TINITALY/01: a new triangular irregular network of Italy, 3. Ann Geophys 2007;50 (3):407–25. https://doi.org/10.4401/ag-4424.

[43] Gasperini L, Marzocchi A, Mazza S, Miele R, Meli M, Najjar H, Michetti AM, Polonia A. Morphotectonics and late Quaternary seismic stratigraphy of Lake Garda (northern Italy). Geomorphology 2020;371:107427. https://doi.org/10.1016/j.geomorph.2020.107427.

[44] Fuganti A. Valutazioni geologiche ed idrogeologiche sulle caratteristiche e sull'origine dell'acqua minerale naturale fonte Linfano. In: Provincia Autonoma di Trento; 2008.

[45] Poletto F, Corubolo P, Farina B, Meneghini F, Petronio L, Maffione S, Barbagallo A. Rilevo VSP pozzo Arco 1 - rapporto finale. Rel. OGS no. 2013/13 Sez. GEO 3, Istituto Nazionale di Oceanografia e di Geofisica Sperimentale. 2013.

[46] Ibs-von Seht M, Wohlenberg J. Microtremor measurements used to map thickness of soft sediments. Bull Seismol Soc Am 1999;89(1):250–9. https://doi.org/10.1785/BSSA0890010250.

[47] Parolai S, Bormann P, Milkereit C. New relationships between Vs, thickness of sediments, and resonance frequency calculated by the H/V ratio of seismic noise for the Cologne area (Germany). Bull Seismol Soc Am 2002;92(6):2521–7. https://doi.org/10.1785/0120010248.

[48] Thabet M. Site-specific relationships between bedrock depth and HVSR fundamental resonance frequency using KiK-NET data from Japan. Pure Appl Geophys 2019;176(11):4809–31. https://doi.org/10.1007/s00024-019-02256-7.

[49] PAT. Geocatalogue of the autonomous province of trento. 2025.

[50] Gosar A, Lenart A. Mapping the thickness of sediments in the Ljubljana moor basin (Slovenia) using microtremors. Bull Earthq Eng 2010;8(3):501–18. https://doi.org/10.1007/s10518-009-9115-8.

[51] Park, Choon B., Richard D. Miller, and Jianghai Xia. Multichannel Analysis of Surface Waves. GEOPHYSICS 64, no. 3 (1999): 800–808. https://doi.org/10.1190/1.1444590.

[52] Parolai S, Picozzi M, Richwalski SM, Milkereit C. Joint inversion of phase velocity dispersion and H/V ratio curves from seismic noise recordings using a genetic algorithm, considering higher modes. Geophys Res Lett 2005;32(1). https://doi.org/10.1029/2004GL021115.

[53] Boxberger T, Picozzi M, Parolai S. Shallow geology characterization using Rayleigh and Love wave dispersion curves derived from seismic noise array measurements. J Appl Geophys 2011;75(2):345–54. https://doi.org/10.1016/j.jappgeo.2011.06.032.

[54] LaFehr TR. Standardization in gravity reduction. Geophysics 1991;56(8):1170–8. https://doi.org/10.1190/1.1443137.

[55] LaFehr TR. An exact solution for the gravity curvature (Bullard B) correction. Geophysics 1991;56(8):1179–84. https://doi.org/10.1190/1.1443138.

[56] Banerjee B, Das Gupta SP. Gravitational attraction of a rectangular parallelepiped. Geophysics 1977;42(5):1053–5. https://doi.org/10.1190/1.1440766.

[57] Cordell L, McCafferty AE. A terracing operator for physical property mapping with potential field data. Geophysics 1989;54(5):621–34. https://doi.org/10.1190/1.1442689.

[58] Anikiev D, Götze H-J, Plonka C, Scheck-Wenderoth M, Schmidt S, Götze H-J, Schmidt S. IGMAS+: interactive gravity and magnetic application system. GFZ Data Services; 2023.

[59] Li Y, Oldenburg DW. 3-D inversion of gravity data. Geophysics 1998;63(1):109–19. https://doi.org/10.1190/1.1444302.

[60] Akimbekova A, Trippetta F, Carboni F, Pauselli C, Maletti GM, Casero A, Miranda F, Barchi MR. Deriving Vp velocity and density properties of complex litho-structural units from the analysis of geophysical log data: a study from the Southern Apennines of Italy. Mar Petrol Geol 2024;160:106634. https://doi.org/10.1016/j.marpetgeo.2023.106634.

[61] Shynkarenko A, Kremer K, Stegmann S, Bergamo P, Lontsi AM, Roesner A, Hammerschmidt S, Kopf A, Fäh D. Geotechnical characterization and stability analysis of subaqueous slopes in Lake Lucerne (Switzerland). Nat Hazards 2022; 113(1):475–505. https://doi.org/10.1007/s11069-022-05310-1.

[62] Paolucci R, Mazzieri I, Smerzini C. Anatomy of strong ground motion: near-source records and three-dimensional physics-based numerical simulations of the Mw 6.0 2012 May 29 Po plain earthquake, Italy. Geophys J Int 2015;203(3):2001–20. https://doi.org/10.1093/gji/ggv405.

[63] Morozov IB. On the relation between bulk and shear seismic dissipation. Bull Seismol Soc Am 2015;105(6):3180–8. https://doi.org/10.1785/0120150093.

[64] Seriani G, Priolo E. Spectral element method for acoustic wave simulation in heterogeneous media. Finite Elem Anal Des 1994;16(3):337–48. https://doi.org/10.1016/0168-874X(94)90076-0.

[65] Savage B, Komatitsch D, Tromp J. Effects of 3D attenuation on seismic wave amplitude and phase measurements. Bull Seismol Soc Am 2010;100(3):1241–51. https://doi.org/10.1785/0120090263.

[66] Primofiore I, Baron J, Klin P, Laurenzano G, Muraro C, Capotorti F, Amanti M, Vessia G. 3D numerical modelling for interpreting topographic effects in rocky hills for Seismic Microzonation: the case study of Arquata del Tronto hamlet. Eng Geol 2020;279:105868. https://doi.org/10.1016/j.enggeo.2020.105868.

[67] Ajala R, Persaud P, Juarez A. Earth model-space exploration in southern California: influence of topography, geotechnical layer, and attenuation on wavefield accuracy. Front Earth Sci 2022;10. https://doi.org/10.3389/feart.2022.964806.

[68] Baron J, Primofiore I, Klin P, Vessia G, Laurenzano G. Investigation of topographic site effects using 3D waveform modelling: amplification, polarization and torsional motions in the case study of Arquata del Tronto (Italy). Bull Earthq Eng 2022;20 (2):677–710. https://doi.org/10.1007/s10518-021-01270-2.

[69] Ba Z, Zhao J, Zhu Z, Zhou G. 3D physics-based ground motion simulation and topography effects of the 05 September 2022 *M*W6.6 Luding earthquake, China. Soil Dynam Earthq Eng 2023;172:108048. https://doi.org/10.1016/j.soildyn.2023.108048.

[70] Chaljub E, et al. 3-D numerical simulations of earthquake ground motion in sedimentary basins: testing accuracy through stringent models. Geophys J Int 2015;201(1):90–111. https://doi.org/10.1093/gji/ggu472.

[71] Maufroy E, et al. 3D numerical simulation and ground motion prediction: verification, validation and beyond – lessons from the E2VP project. Soil Dynam Earthq Eng 2016;91:53–71. https://doi.org/10.1016/j.soildyn.2016.09.047.

[72] Ayoubi P, Mohammadi K, Asimaki D. A systematic analysis of basin effects on surface ground motion. Soil Dynam Earthq Eng 2021;141:106490. https://doi.org/10.1016/j.soildyn.2020.106490.

[73] Kawase H, Sánchez-Sesma FJ, Matsushima S. The optimal use of horizontal-to-vertical spectral ratios of earthquake motions for velocity inversions based on

diffuse-field theory for plane waves. Bull Seismol Soc Am 2011;101(5):2001–14. https://doi.org/10.1785/0120100263.

[74] Hartzell SH. Site response estimation from earthquake data. Bull Seismol Soc Am 1992;82(6):2308–27. https://doi.org/10.1785/BSSA0820062308.

[75] Oth A, Bindi D, Parolai S, Di Giacomo D. Spectral analysis of K-NET and KiK-net data in Japan, part II: on attenuation characteristics, source spectra, and site response of borehole and surface stations. Bull Seismol Soc Am 2011;101(2): 667–87. https://doi.org/10.1785/0120100135.

[76] Klin P, Laurenzano G, Priolo E. GITANES: a MATLAB package for estimation of site spectral amplification with the generalized inversion technique. Seismol Res Lett 2018;89(1):182–90. https://doi.org/10.1785/0220170080.

[77] Klin P, Laurenzano G, Barnaba C, Priolo E, Parolai S. Site amplification at permanent stations in Northeastern Italy. Bull Seismol Soc Am 2021;111(4): 1885–904. https://doi.org/10.1785/0120200361.

[78] Borcherdt RD. Effects of local geology on ground motion near San Francisco Bay. Bull Seismol Soc Am 1970;60(1):29–61. https://doi.org/10.1785/BSSA0600010029.

[79] Asimaki D, Shi J. SeismoSoil user manual, v1.3. GeoQuake Research Group, California Institute of Technology; 2017.

[80] Anderson JG. Quantitative measure of the goodness-of-fit of synthetic seismograms. In: *13 th world conference on earthquake engineering* Vancouver; 2004. B.C., Canada.

[81] Roten D, Olsen KB, Pechmann JC. 3D simulations of M 7 earthquakes on the Wasatch fault, Utah, part II: broadband (0–10 hz) ground motions and nonlinear soil behavior. Bull Seismol Soc Am 2012;102(5):2008–30. https://doi.org/10.1785/0120110286.

[82] Paolucci R, Gatti F, Infantino M, Smerzini C, Güney Özcebe A, Stupazzini M. Broadband ground motions from 3D physics-based numerical simulations using artificial neural networks. Bull Seismol Soc Am 2018;108(3A):1272–86. https://doi.org/10.1785/0120170293.

[83] Wessel P, Luis JF, Uieda L, Scharroo R, Wobbe F, Smith WHF, Tian D. The generic mapping tools version 6. G-cubed 2019;20(11):5556–64. https://doi.org/10.1029/2019GC008515.